



Representation of the Convectively Coupled Kelvin Waves in Modern Reanalysis Products[©]

MU-TING CHIEN^a AND DAEHYUN KIM^{©a}

^a Department of Atmospheric Sciences, University of Washington, Seattle, Washington

(Manuscript received 17 March 2022, in final form 22 September 2022)

ABSTRACT: This study aims to deepen our understanding of the destabilization mechanisms and the mean-state modulation of the convectively coupled Kelvin waves (CCKWs) while testing simple models for CCKWs. We examine CCKW precipitation, vertical structure, and energetics in four modern reanalyses: the fifth version of ECMWF Reanalysis (ERA5), NASA Modern-Era Retrospective Analysis for Research and Applications, version 2 (MERRA-2), the second version of the NCEP Climate Forecast System Reanalysis (CFSR), and the Japanese 55-year Reanalysis (JRA-55). The CCKW precipitation signal strength in the wavenumber–frequency domain and the geographical distribution of CCKW precipitation variability are reasonably represented in all reanalyses, although they commonly underestimate the amplitude of CCKW precipitation. Despite considerable interreanalysis differences in the vertical structure of temperature and diabatic heating anomalies, the eddy available potential energy (EAPE) generation within the CCKWs is found to be associated with the second baroclinic mode whereas the first baroclinic mode damps CCKW EAPE in three out of four reanalyses. Geographically, strong CCKW activity occurs in the areas of high mean-state sea surface temperature (SST), where the second mode EAPE generation is higher, mainly due to a stronger stratiform heating and a tighter wave–convection coupling. Our results are supportive of the simple models for CCKWs in which CCKWs are destabilized within the second baroclinic mode component.

KEYWORDS: Convective storms/systems; Kelvin waves; Tropical variability

1. Introduction

Over the tropics, deep cumulus clouds are often organized into different temporal and spatial scales. Among the envelop disturbances are the convectively coupled equatorial waves (CCEWs), which include the convectively coupled Kelvin waves (CCKWs), the westward and eastward inertial–gravity waves (WIG and EIG, respectively), the equatorial Rossby waves (ER), and the mixed Rossby–gravity waves (MRG) (Kiladis et al. 2009). Their signature in the wavenumber–frequency power spectrum of precipitation or other proxies for deep convection follows the dispersion relationships of their corresponding dry waves (Matsuno 1966), albeit with lower equivalent depths relative to that of the dry waves.

Among the family of CCEWs, CCKWs are unique in a few aspects. First, CCKWs always propagate eastward. Second, CCKWs are the only nondispersive waves among the Matsuno modes; the phase speed of the dry KWs is constant for a

given equivalent depth. Last, the fluctuations of precipitation anomalies associated with CCKWs cover a wide range in terms of both temporal (periods of 2.5–20 days) and spatial (zonal wavelengths of 3000–10 000 km) scales.

CCKWs have profound impacts on local weather and low-frequency modes of variability in the tropics. They bring extreme rainfall and severe flooding events to Indonesia (Murata et al. 2006; Latos et al. 2021), South America (Wang and Fu 2007; Liebmann et al. 2009), and Africa (Mekonnen et al. 2008; Sinclair et al. 2015). CCKWs affect tropical cyclogenesis in the Indian Ocean (Bessafi and Wheeler 2006) and the onset of the summer monsoon over the South China Sea (Straub et al. 2006) and India (Flatau et al. 2003). CCKWs also interact with large-scale low-frequency phenomena including the Madden–Julian oscillation (MJO) (Roundy 2008) and El Niño–Southern Oscillation (Straub et al. 2006).

Despite the broad impact of CCKWs on Earth's weather–climate system, the fidelity of CCKW simulation in current global climate models (GCMs) is still unsatisfactory (Lin et al. 2006; Straub et al. 2010; Benedict et al. 2013; Hung et al. 2013). The poor representation of CCKWs in GCMs could stem from the biases in the basic state or the errors in the internal dynamics of CCKWs, meaning that improving the representation of CCKWs requires a deep understanding of how CCKW activity is modulated by environmental conditions

[©] Supplemental information related to this paper is available at the Journals Online website: <https://doi.org/10.1175/JAS-D-22-0067.s1>.

Corresponding author: Daehyun Kim, daehyun@uw.edu

and how CCKWs grow against frictional damping in the atmosphere. Unfortunately, we still do not have a complete understanding of the two aspects of CCKW variability, which are related to each other.

Regarding the basic-state control over CCKW activity, studies have shown that CCKWs are active in tropical regions in the eastern Indian Ocean, the western and central Pacific Ocean, and the North Atlantic Ocean (Kiladis et al. 2009) with considerable seasonal variation (Yang et al. 2007). They also showed that the basic state in the CCKW-active regions is characterized by relatively high sea surface temperature (SST) (Straub and Kiladis 2002; Roundy and Frank 2004; Yang et al. 2007; Wang and Chen 2016). While studies have shown that warm underlying SST provides a favorable condition for CCKW development, the pathways through which the mean-state SST affects CCKW growth and maintenance remain unclear. Among the questions that have not been fully answered is, How exactly does warm SST affect the coupling of convection with the dry KW? A careful examination of the kinematics and thermodynamics of CCKWs could provide useful insights.

The above question about the relationship between the basic state and CCKW activity is also asking questions related to the internal dynamics of CCKWs, especially the destabilization mechanism. In other words, understanding the instability mechanism of CCKWs is key to understanding the role of the basic state on the regionality and seasonality of CCKW activity (Yasunaga 2011). A number of theoretical models have been proposed to explain the scale selection and instability mechanisms of CCKWs, which can be grouped into two schools of thought that emphasize either the first baroclinic mode (e.g., Lindzen 1974; Emanuel 1987; Raymond and Fuchs 2007) or the second baroclinic mode (e.g., Mapes 2000; Khouider and Majda 2006; Kuang 2008) as the essential component. While in both groups CCKWs are hypothesized to grow through the generation of the eddy available potential energy (EAPE; Lorenz 1955), different vertical mode (first versus s baroclinic mode) is hypothesized to be in charge of EAPE generation in the two groups of CCKW theories. It remains unknown which vertical mode is more important in energizing CCKWs and therefore is key to the destabilization of CCKWs. In this situation, a diagnosis of EAPE growth rate associated with the first and second baroclinic modes in observations would be extremely useful for testing the simple models of CCKWs.

The goal of the present study is to thoroughly examine CCKW precipitation, vertical structure, and energetics—EAPE growth rate associated with the first and second baroclinic modes—in four modern reanalyses: the fifth major global reanalysis produced by the European Centre for Medium-Range Weather Forecasts (ECMWF) Reanalysis (ERA5) (Hersbach et al. 2020), the National Aeronautics and Space Administration (NASA) Modern-Era Retrospective Analysis for Research and Applications, version 2 (MERRA-2) (Gelaro et al. 2017), the second version of the National Centers for Environmental Prediction (NCEP) Climate Forecast System Reanalysis (CFSR) (Saha et al. 2014), and the Japanese 55-year Reanalysis (JRA-55) (Kobayashi et al. 2015). The reanalysis products provide

the best estimates of the atmospheric state variables and the radiative and turbulent fluxes in the global domain for the past few decades, serving as an indispensable tool to study various atmospheric phenomena. Through a careful examination of various CCKW characteristics, we aim to deepen our understanding of CCKWs, with a particular focus on investigating the basic-state SST control of the geographical and seasonal variation of CCKWs and testing the simple models for CCKWs.

While analyzing multiple reanalyses, we also aim to compare the representation of CCKWs between them. Because each reanalysis has its own strengths and weaknesses depending on the forecast model and data assimilation scheme employed, it is critical to know the uncertainty in the reanalyses. Previous studies have documented the difference between reanalyses in many aspects, including the quasi-biennial oscillation winds (Long et al. 2017), tropical diabatic heating profiles (Ling and Zhang 2013), the moist static energy budget of the Madden-Julian oscillation (Ren et al. 2021), and subseasonal precipitation variability (Kim et al. 2014). Kim et al. (2014) examined CCKW precipitation variability in the antecedent versions of the reanalyses used here, showing that CCKW precipitation in the reanalyses presents substantial biases when compared to satellite products. Our study further examines whether modern versions of the reanalyses improve the representation of CCKW precipitation. To our knowledge, our study is the first one that documents CCKW vertical structure and energetics in multiple reanalyses.

By examining and comparing the representation of CCKWs in multiple reanalyses, we aim to answer the following three questions: 1) Are CCKWs destabilized within the first or second baroclinic mode component? 2) How are CCKWs modulated by the mean-state sea surface temperature? 3) How well do modern reanalysis products represent CCKWs?

The remainder of this paper is structured as follows. Section 2 describes the reanalysis products and observations used in this study and how we quantify the EAPE growth rate associated with the first and second barocline modes. Section 3 presents the intercomparison of CCKW precipitation, vertical structure, and energetics in reanalyses. The summary and conclusions are given in section 4.

2. Data and methods

a. Reanalysis and observational data

The primary datasets for our analysis are various atmospheric field variables from ERA5, MERRA-2, CFSR, and JRA-55 products. Horizontal wind, vertical pressure velocity, temperature, geopotential, and specific humidity are used to analyze the vertical structure and energetics of CCKWs. Precipitation from each reanalysis is also used to characterize convective activity associated with CCKWs. The mean-state column relative humidity is calculated by the average among four reanalysis products. A brief description of the four reanalyses used in our study is presented in Table 1. For four-dimensional variables, we discard data above 100 hPa and select the common vertical levels among four reanalyses,

TABLE 1. A brief description of the global reanalysis products used in this study.

Name (organization)	Availability	Assimilation scheme	Horizontal resolution ($^{\circ}$)	Reference
ERA5 (ECMWF)	1979–present	4D-Var	0.28125×0.28125	Hersbach et al. (2020)
MERRA-2 (NASA GMAO)	1980–present	3D-Var	0.5×0.625	Gelaro et al. (2017)
CFSR, version 2 (NCEP)	2011–present	3D-Var	0.5×0.5	Saha et al. (2014)
JRA-55 (JMA)	1958–present	4D-Var	0.5×0.5	Kobayashi et al. (2015)

retaining 22 vertical levels from 962.5 to 125 hPa (1000-hPa level is dropped to avoid missing values when sea level pressure is below 1000 hPa). To avoid using artificially extrapolated data under topography, we exclude the land data and focus on the tropical oceans from 15°S to 15°N , where CCKW precipitation amplitude maximizes (e.g., Kiladis et al. 2009).

Three sets of observational datasets are used to evaluate the performance of the reanalyses. For precipitation, the Tropical Rainfall Measuring Mission (TRMM) product 3B42, version 7, product (Huffman et al. 2007) is used. The vertical structure of temperature, specific humidity, geopotential, and wind anomalies associated with CCKWs in the central Pacific are compared to those from the radiosonde-sounding data in Majuro (7.0683°N , 171.2942°E) from Integrated Global Radiosonde Archive (Durre et al. 2006). We also use SST from Hadley Centre Sea Ice and Sea Surface Temperature (HadISST) dataset (Rayner et al. 2003). All data are obtained for the period covered by all reanalyses (2011–18) and gridded onto daily and $2.5^{\circ} \times 2.5^{\circ}$ resolution.

b. Space–time spectral analysis

To investigate CCKW characteristics in the wavenumber-frequency domain, we perform the space–time spectral analysis (Wheeler and Kiladis 1999; Inoue et al. 2020). Our method closely follows that of Wheeler and Kiladis (1999). With the segment length of 96 days and the overlapping length of 60 days, we obtain 78 segments from the 8-yr period. As each segment yields 2 degrees of freedom, the total number of degrees of freedom is 156. The edges of each segment are tapered with a 5-day Hann window. The land grid points are excluded from the from spectral analyses following Inoue et al. (2020), who first put a nonnumber to all land grids and then replaced the nonnumbers with zero after separating the resulting data into the antisymmetric and symmetric components.

Specifically, we calculate the normalized space–time power spectrum of precipitation (Fig. 2) and the cross spectra of temperature and diabatic heating (Fig. 4). The normalization of the precipitation power spectrum is done by 15 passes of 1–2–1 running-mean filter over frequencies and zonal wavenumbers separately over the average of the symmetric and antisymmetric power spectrum of precipitation. Also, CCKW-related anomalies are isolated using Fourier filtering, again following Wheeler and Kiladis (1999). The Fourier filtering retains only wave components within the CCKW band (frequencies 2.5–20 days, zonal wavenumbers 1–14, and the equivalent depths 8–90 m, indicated in Fig. 2 with purple lines).

c. CCKW vertical structure

The composite vertical structure of CCKWs is obtained by regressing atmospheric field variables upon CCKW-filtered precipitation on each latitude–longitude grid point. Later, we composite CCKW vertical structure based on the mean-state SST values on each grid (e.g., Figs. 11–13 and 15). For the SST-based composites, we use SST from HadISST. ERA5, MERRA-2, and JRA-55 were generated by prescribing the observed SST and therefore HadISST is suitable to represent the SST in these reanalyses. For CFSR, although it was generated from an ocean–atmosphere coupled model, we verified that the SST field in CFSR showed only small deviations from that of HadISST, with an average bias over the Indo-Pacific warm pool being $\sim 0.05^{\circ}\text{C}$ (not shown).

d. Empirical vertical mode decomposition

The vertical structures of the first and second baroclinic modes are obtained empirically (e.g., Adames and Wallace 2014; Inoue et al. 2020) via the empirical orthogonal function (EOF) analysis. The diabatic heating Q , denoted as apparent heating Q_1 in Yanai et al. (1973), is obtained as the residual in the dry static energy (S) budget, formulated as

$$Q = \frac{\partial S}{\partial t} + u \frac{\partial S}{\partial x} + v \frac{\partial S}{\partial y} + \omega \frac{\partial S}{\partial p}, \quad (1)$$

where S is the sum of enthalpy ($C_p T$) and geopotential (gz),

$$S = C_p T + gz. \quad (2)$$

Daily anomalies of Q and T are obtained by subtracting the climatological seasonal cycle, which is the sum of the annual mean and the first three annual harmonics. In the following, Q and T represent daily anomalies if not specified otherwise.

We perform EOF analysis of Q so that it is decomposed into the empirical orthogonal vertical structure functions (EOFs) and their associated principal components (PCs; with a hat on top of the variable denotes its PCs) that represent spatial and temporal variability:

$$Q(x, y, p, t) = \sum_{i=1}^N \text{EOF}_i^Q(p) \times \hat{Q}_i(x, y, t), \quad (3)$$

where the subscript indicates the i th EOF or the corresponding PC and N denotes the size of the EOF matrix.

Figure 1 shows the vertical structures of the first and second EOFs from each reanalysis over the tropical (15°S – 15°N) ocean. The first EOF (EOF1) exhibits a single-signed structure throughout the troposphere (Fig. 1a) while the second

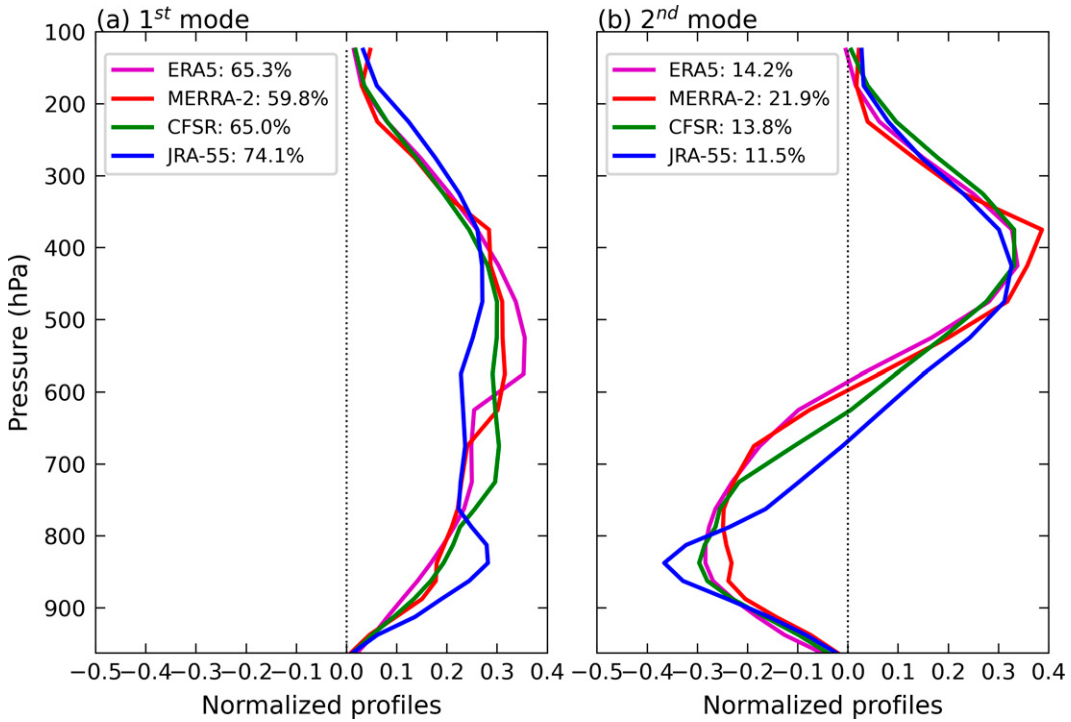


FIG. 1. Vertical profiles of the (a) first and (b) second EOFs of the diabatic heating anomalies over the tropical (15°S – 15°N) ocean. The percentage of the explained variance of each mode is shown in the legend.

EOF (EOF2) shows a dipole structure (Fig. 1b), resembling the perceived structure of the first and second baroclinic modes, respectively (e.g., Fulton and Schubert 1985; Haertel et al. 2008; Adames and Wallace 2014; Inoue et al. 2020). While the first baroclinic mode is associated with the deep convective clouds, the second baroclinic mode is associated with stratiform clouds. In this paper, when we mention the deep convective and the stratiform clouds, we are specifically referring to the first and second baroclinic modes, respectively. While there are some differences among reanalyses in the structure of EOF1 and EOF2, the gross structure of the two leading EOFs is similar. The explained variance of each mode varies up to 10% for different reanalyses, with the explained variance of the first EOF mode being largest and smallest in JRA-55 and MERRA-2, respectively, while the opposite is true for the second EOF mode. Nevertheless, the two leading modes together capture most of the total variance in diabatic heating in all reanalyses.

Diabatic heating can therefore be truncated into the leading two EOF modes as follows:

$$Q(x, y, p, t) \sim \sum_{i=1}^2 \text{EOF}_i^Q(p) \times \hat{Q}_i(x, y, t). \quad (4)$$

Although the leading EOFs of T have the vertical structure that is distinct from those of Q , we assume for simplicity that diabatic heating and temperature have the same vertical structure as in Haertel et al. (2008), who considered 2D gravity waves with a rigid lid at 100 hPa. EOFs obtained from Q are used to derive PCs for T denoted as \hat{T} :

$$T(x, y, p, t) \sim \sum_{i=1}^2 \text{EOF}_i^Q(p) \times \hat{T}_i(x, y, t). \quad (5)$$

e. Quantifying EAPE growth rate in the physical domain

The concept of the available potential energy (APE) was developed by Lorenz (1955). EAPE is APE for “eddies,” which is defined here as daily temporal anomalies. EAPE is describing the difference between the total eddy potential energy and the minimum total eddy potential energy, which could be reached through adiabatic redistribution of air masses. EAPE is formulated as

$$E = \int_0^{p_s} \frac{1}{2} \frac{\overline{T^2}}{(\Gamma_d - \bar{\Gamma})\tilde{T}} dp, \quad (6)$$

where \tilde{T} is the daily domain mean temperature profile without removing seasonal cycles, Γ is the environmental temperature lapse rate, Γ_d is the dry adiabatic lapse rate, and overbar denotes the time mean. The EAPE budget has been used to investigate the energetics of convectively coupled equatorial waves in past studies (e.g., Nitta 1972; Chen et al. 2016; Nakamura and Takayabu 2022). In the EAPE budget equation, there are two source terms (generation from diabatic heating and conversion from mean-state APE) and one sink term (conversion to eddy kinetic energy). We focus on generation of EAPE from diabatic heating in this study because past studies have shown that generation of EAPE from diabatic heating is the dominant source of EAPE within

CCKWs and other tropical synoptic waves, while conversion from the mean-state APE is negligible (one or two orders of magnitude smaller than the EAPE generation) (e.g., Nitta 1972; Chen et al. 2016; Nakamura and Takayabu 2022).

Meanwhile, as mentioned in section 1, the simple models which have been proposed to explain the instability mechanism of CCKWs (e.g., Lindzen 1974; Emanuel 1987; Raymond and Fuchs 2007; Mapes 2000; Khouider and Majda 2006; Kuang 2008) all hypothesize that CCKWs grow by EAPE generation either associated with the first or second mode. The analytical solutions of these simple models present characteristics that are similar to those of the observed CCKWs, including the spatial-temporal scales, propagation speed, and vertical structure. If the analytical solutions of the simple models are a manifestation of the observed CCKWs, the generation of EAPE due to diabatic heating should be a key growing mechanism of the CCKWs.

The generation of EAPE from diabatic heating (G) takes the following form:

$$G = \int_0^{p_s} \frac{\overline{QT}}{(\Gamma_d - \bar{\Gamma})\bar{T}} dp. \quad (7)$$

In Eq. (7), G is proportional to the covariance of diabatic heating and temperature. Last, we define the growth rate (σ) for EAPE as G normalized by EAPE:

$$\sigma = G/E, \quad (8)$$

which we consider as a proxy for the growth rate of CCKWs due to EAPE production. Values of σ for the first (σ_1) and second (σ_2) baroclinic modes are obtained using CCKW-filtered PCs (\hat{Q}'_i and \hat{T}'_i):

$$\sigma_i = 2 \frac{\hat{Q}'_i \hat{T}'_i}{\hat{T}'_i^2}, \quad i = 1 \text{ or } 2. \quad (9)$$

We calculate σ_i at each latitude-longitude grid and match with the geographies of CCKW activities to test the hypothesis of whether CCKWs grow by EAPE generation associated with the first or second mode. Although we think that the evidence presented in this section is enough to motivate testing our hypothesis, we have also verified that TRMM precipitation and EAPE generation in all reanalyses is highly coherent over CCKW band (Fig. S1 in the online supplemental material). This suggests that EAPE generation is closely relevant to precipitation variability in all reanalyses and therefore investigating EAPE generation in reanalyses is a suitable framework to understand CCKW precipitation anomalies.

f. Quantifying EAPE growth rate in the wavenumber-frequency domain

Another way to test the hypothesis of whether CCKWs grow by EAPE generation associated with the first or second mode is to investigate the relationship between EAPE growth rate and CCKW activity in the wavenumber-frequency space. For this purpose, we calculate σ_1 and σ_2 in the wavenumber-

frequency domain by Fourier-transformed PCs, denoted as $\hat{Q}_1^{f,k}$, $\hat{Q}_2^{f,k}$, $\hat{T}_1^{f,k}$, and $\hat{T}_2^{f,k}$ (section 2b), where the superscript f denotes frequency and k denotes zonal wavenumber. To simplify the notation, the covariance between diabatic heating and temperature is denoted as

$$\langle QT \rangle_i^{f,k} = \langle \hat{Q}_i^{f,k} \hat{T}_i^{f,k*} \rangle, \quad (10)$$

and the respective variances of diabatic heating and temperature as

$$\langle TT \rangle_i^{f,k} = \langle \hat{T}_i^{f,k} \hat{T}_i^{f,k*} \rangle \quad \text{and} \quad \langle QQ \rangle_i^{f,k} = \langle \hat{Q}_i^{f,k} \hat{Q}_i^{f,k*} \rangle, \quad (11)$$

where angle brackets denote the average over latitude and over each time-longitude segment smoothed with a single pass of a 1–2–1 running-mean filter over frequencies and zonal wavenumbers separately, and the star denotes complex conjugate.

The growth rate for the first and second baroclinic modes is formulated as

$$\sigma_i = 2 \times \frac{\text{real}(\langle QT \rangle_i^{f,k})}{\langle TT \rangle_i^{f,k}}, \quad i = 1 \text{ or } 2, \quad (12)$$

where taking the real part remains only the in-phase and out-of-phase components of the covariance between diabatic heating and temperature, which contribute to the positive and negative growth rate. To aid in interpreting the results of the growth rate calculation, we investigate the phase difference φ and coherence squared (Coh^2) between diabatic heating and temperature.

The phase difference φ between diabatic heating and temperature is obtained by

$$\varphi_i = \tan^{-1} \left(\frac{\text{imag}\{\langle QT \rangle_i^{f,k}\}}{\text{real}\{\langle QT \rangle_i^{f,k}\}} \right), \quad i = 1 \text{ or } 2. \quad (13)$$

The coherence squared (Coh^2), quantifying the robustness of the phase relationship between diabatic heating and temperature, is defined as

$$\text{Coh}_i^2 = \frac{\text{real}\{\langle QT \rangle_i^{f,k}\}^2 + \text{imag}\{\langle QT \rangle_i^{f,k}\}^2}{\langle QQ \rangle_i^{f,k} \langle TT \rangle_i^{f,k}}, \quad i = 1 \text{ or } 2. \quad (14)$$

Coh^2 values greater than 0.03 are statistically significant at the 99% confidence level under the chi-squared statistical test with a degree of freedom of 156. For the following discussion, we will focus on the EAPE growth rate where $\text{Coh}^2 > 0.03$.

3. Results

a. CCKW precipitation

Before examining the energetics and vertical structure of CCKWs, we analyze in this subsection the precipitation variability associated with the CCKWs to see if it is reasonably represented in the reanalysis products. In our analysis below, precipitation is used as a proxy for convection, which is a key component of the CCKWs. Since each reanalysis represents

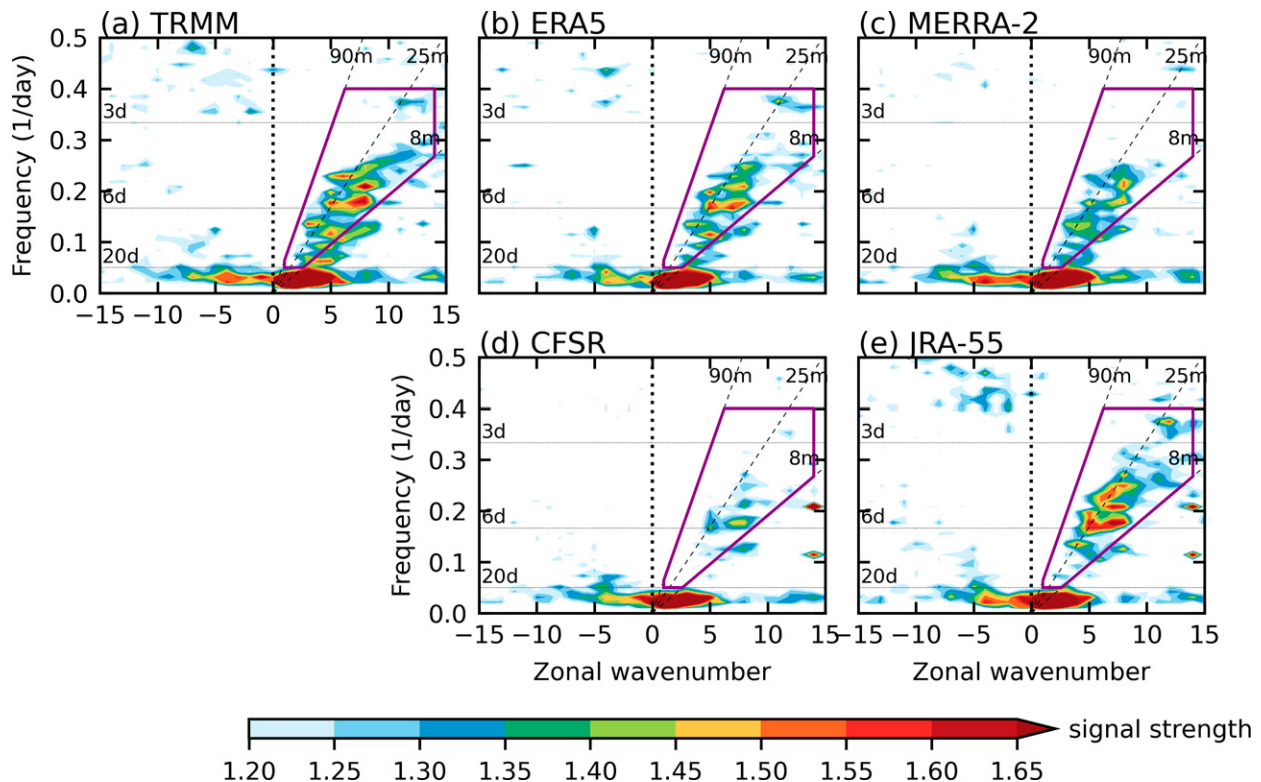


FIG. 2. Symmetric component of the normalized wavenumber–frequency power spectrum of precipitation over tropical (15°S – 15°N) ocean from (a) TRMM, (b) ERA5, (c) MERRA-2, (d) CFSR, and (e) JRA-55. The purple polygon indicates the CCKW band (zonal wavenumbers 1–14, frequencies 2.5–20 days, and equivalent depths 8–90 m).

convection processes differently depending on its model dynamics and physics, it is worthwhile to examine how CCKW precipitation is represented in each reanalysis in both the wavenumber–frequency domain and the physical domain.

Figure 2 shows the normalized space–time power spectrum of equatorial precipitation, denoted as the signal strength. The signal strength is essentially the ratio of precipitation variance at a specific temporal and spatial scale to that of the background random noise. Only the symmetric component is shown as our focus is on the CCKWs. In observations, signal strength greater than 1.4 (statistically significant at the 95% confidence level based on an *F* test) appears within the CCKW band (Fig. 2a). The statistically significant signal strength within the CCKW band suggests that CCKWs grow in amplitude against frictional dissipation or other damping processes at least in some stages of their life cycle. ERA5, MERRA-2, and JRA-55 reasonably capture the spatial and temporal scales of the CCKWs, with statistically significant signal strength (>1.4) appearing along the $h = 25\text{ m}$ dispersion line and within periods of 4–10 days and zonal wavenumbers of 3–10 as in observations. On the contrary, the signal strength within the CCKW band is somewhat underestimated in CFSR.

The geographical distribution of the standard deviation of CCKW daily precipitation anomalies is shown in Fig. 3. Pronounced precipitation variability associated with CCKWs can be found over a relatively warm body of water, with four distinct hotspots in the eastern Indian Ocean, southern western Pacific, northern central Pacific, and northern Atlantic, in agreement

with past studies (Roundy and Frank 2004; Masunaga 2007; Mekonnen et al. 2008; Kiladis et al. 2009). The geographical distribution of CCKW precipitation variability, including the positions of the four hotspots, is reasonably captured in the reanalyses, although the magnitude of CCKW precipitation variability is somewhat underestimated in CFSR and JRA-55.

Figures 2 and 3 collectively show that the modern reanalyses reasonably represent CCKW precipitation variability in the wavenumber–frequency (Fig. 2) and the physical (Fig. 3) space, with ERA5 and MERRA-2 exhibiting relatively good performance in terms of the signal strength and the magnitude of CCKW precipitation anomalies.

b. EAPE growth rate in the wavenumber–frequency domain

In this subsection, we diagnose the CCKW EAPE growth rate associated with the two vertical modes in the wavenumber–frequency domain. Assuming that the maintenance of CCKWs can be explained by that of EAPE (e.g., Lindzen 1974; Emanuel 1987; Raymond and Fuchs 2007; Mapes 2000; Khouider and Majda 2006; Kuang 2008), the EAPE growth rate quantifies how an initial disturbance triggered by some random processes would develop; if the EAPE growth rate is positive, the initial disturbances would likely amplify, whereas the initial disturbances would damp with a negative EAPE growth rate. Therefore, one would expect to observe positive and large EAPE growth rates within the temporal–spatial scale of the high CCKW precipitation signal strength.

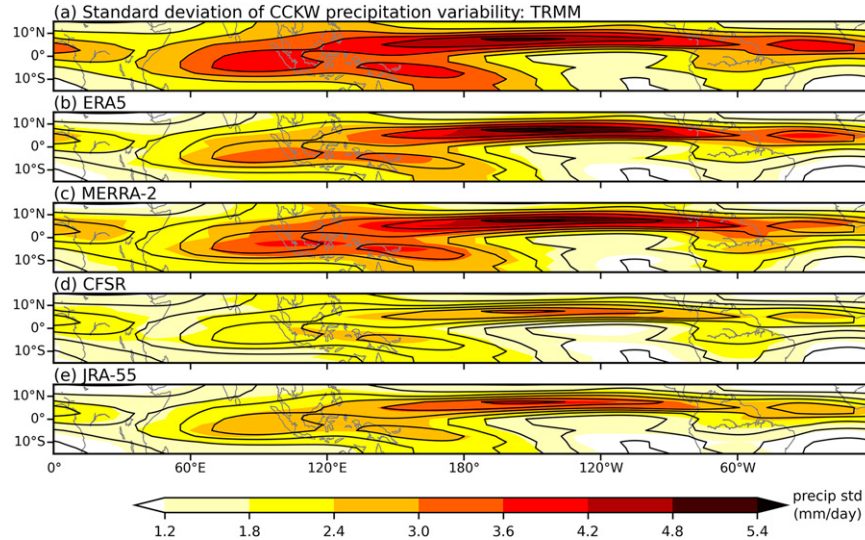


FIG. 3. The geographical distribution of the standard deviation of CCKW-filtered daily precipitation anomalies from (a) TRMM, (b) ERA5, (c) MERRA-2, (d) CFSR, and (e) JRA-55. The TRMM results are overlayed with black contours in all panels.

Figure 4 shows the EAPE growth rate in the wavenumber-frequency space for the first and second baroclinic modes, together with the coherence squared (orange contours) and the phase relationship (arrows) between diabatic heating and temperature anomalies. Also shown in the figure is the high CCKW precipitation signal strength obtained from TRMM (blue contours, signal strength = 1.4).

The four reanalyses can be grouped into two groups by the sign of the EAPE growth rate associated with the two baroclinic modes over the temporal-spatial scale for high CCKW precipitation signal strength. In ERA5, MERRA-2, and CFSR, it is the second baroclinic mode whose associated EAPE growth rate is positive overlapping the strong CCKWs, with the slightly in-phase relationship between the second mode diabatic heating and temperature, indicated by the upward-pointing arrows and pink shading (Figs. 4a–c, right). In these three reanalyses, on the other hand, the first baroclinic mode EAPE growth rate is overall negative across the whole CCKW band, with the slightly out-of-phase relationship between the first mode diabatic heating and temperature, indicated by the downward-pointing arrows and green shading (Figs. 4a–c, left). The results from these reanalyses indicate that the enhanced CCKW signal strength is closely related to the growth of the second baroclinic mode. JRA-55 is an exception in this regard, which exhibits positive and negative EAPE growth rates associated with the first and second baroclinic modes overlapping high CCKW precipitation signal strength, respectively (Fig. 4d).

Except for JRA-55, all other three reanalyses show that the first mode is damping and the second mode is growing for strong CCKWs. The unique slightly out-of-phase first mode structure and the slightly in-phase second mode structure in CCKWs in three reanalyses are also seen in MRG and EIG in the asymmetric spectrum (not shown), but are not shown in MJO, ER, and TD-type waves, highlighting the importance of the second mode dynamics in the destabilization among the

gravity waves. Our result agrees with [Yasunaga and Mapes \(2012\)](#), who showed that the midtropospheric divergence (indicative of the second mode) is coherent with the rain for the gravity waves (CCKWs, EIG, WIG, MRG), but not for the rotational waves (ER, TD, MJO). [Inoue et al. \(2020\)](#) distinguished gravity waves with rotational waves by their stronger vertical tilting in the vertical velocity field and hypothesized the different instability mechanisms governing the two wave types. With the exception of JRA-55, our results suggest that the scale selection of CCKW precipitation variability in the reanalyses is tightly related to the positive second baroclinic mode EAPE growth rate. It should be noted that in reanalysis data, both data assimilation and model physics affect precipitation variability, presumably with a greater contribution from model physics. Precipitation over the ocean, to our knowledge, is not assimilated in any of the four reanalyses considered in our study ([Saha et al. 2010; Kobayashi et al. 2015; Gelaro et al. 2017; Reichle et al. 2017; Hersbach et al. 2020](#)). This implies that CCKW precipitation over the ocean in reanalyses is largely a product of model dynamics and physics, and data assimilation can only indirectly affect precipitation through interactions with other atmospheric field variables (e.g., temperature and wind). Furthermore, we have verified that the contribution of data assimilation to the second mode EAPE growth rate in MERRA-2 is at least one order of magnitude smaller than that from moist physics (not shown). These suggest that CCKW precipitation variability in reanalysis is primarily affected by model physics, with data assimilation playing a secondary role. Therefore, if EAPE generation is an important physical process that affects the growth of CCKWs, stronger EAPE generation would likely lead to stronger CCKW precipitation signals in reanalyses.

c. EAPE growth rate in the physical domain

In this subsection, we perform the diagnosis of the CCKW EAPE growth rate associated with the two vertical modes in

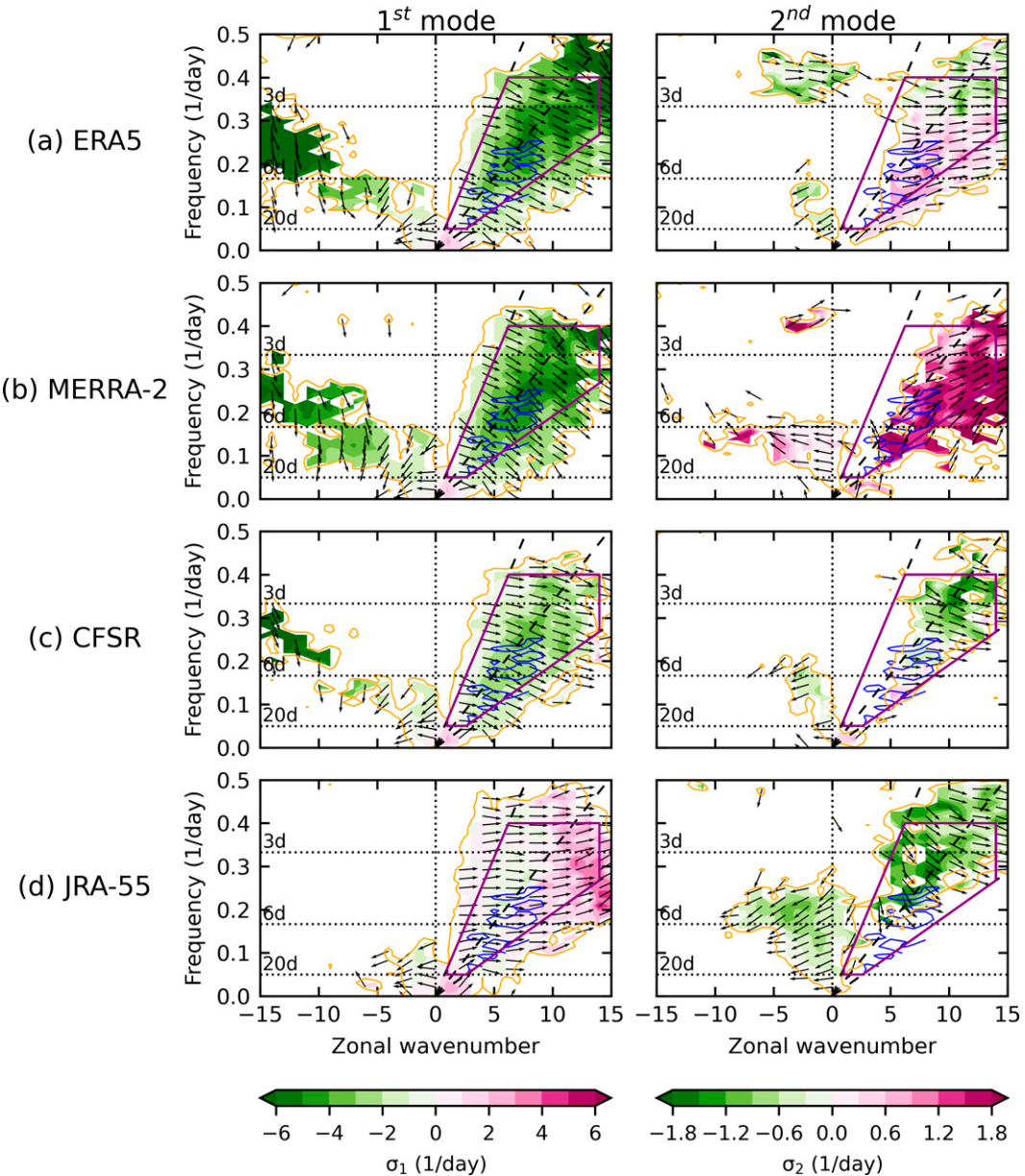


FIG. 4. EAPE growth rate (day^{-1}) for the (left) first and (right) second baroclinic modes from each reanalysis product: (a) ERA5, (b) MERRA-2, (c) CFSR, and (d) JRA-55. Arrows represent the phase relationship between diabatic heating anomalies (Q) and temperature anomalies (T); arrows pointing upward represent T and Q are in phase, downward represent T and Q are out of phase, rightward represent T leads Q by 90°, and leftward represent T lags Q by 90°. Shading denotes the EAPE growth rate, the magnitude of the upward and downward arrows, with upward-pointing arrows in pink shading and downward-pointing arrows in green shading. The polygon consisted with the purple lines indicates the CCKW band (zonal wavenumbers 1–14, frequencies 2.5–20 days, and equivalent depths 8–90 m). The areas within the blue contours are those with the signal strength from TRMM (Fig. 2a) greater than 1.4 within the CCKW band. The orange contours indicate the coherence squared values being 0.03 (statistical significance > 99%). Only the EAPE growth rate and the Q – T relationship that are statistically significant (within orange contours) are shown.

the physical domain. Figures 5 and 6 show the geographical distribution of the first and second mode EAPE growth rates (shading), respectively. Also shown in the figures is the CCKW daily precipitation variance obtained from TRMM

(contours). As in the above subsection, the four reanalyses can be grouped into two groups by the sign of the EAPE growth rate associated with the two baroclinic modes over the Indo-Pacific warm pool regions, where CCKW variability is

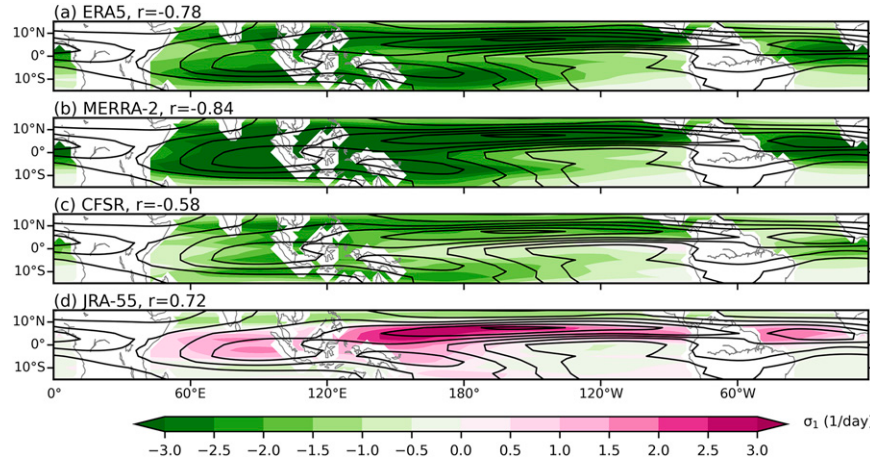


FIG. 5. EAPE growth rate (day^{-1} ; shading) of the first baroclinic mode from each reanalysis product: (a) ERA5, (b) MERRA-2, (c) CFSR, and (d) JRA-55. Black contours indicate the standard deviation of CCKW-filtered daily precipitation anomalies from TRMM (mm day^{-1}). Black contours begin at 1.8 mm day^{-1} with an interval of 0.6 mm day^{-1} . The numbers shown above each panel indicate the pattern correlation coefficient between the standard deviation of CCKW-filtered precipitation anomalies from TRMM and the EAPE growth rate.

pronounced. In ERA5, MERRA-2, and CFSR, it is the second barocline mode whose associated EAPE growth rate is positive over the warm pool regions (Fig. 6), while the first baroclinic mode EAPE growth rate is overall negative (Fig. 5). The results from these reanalyses indicate that the enhanced CCKW variability in the warm pool regions is closely associated with the production of EAPE within the second baroclinic mode. As in Fig. 4, JRA-55 is an exception in this regard, which exhibits positive and negative EAPE growth rates associated with the first and second baroclinic modes in the warm pool regions, respectively.

Figure 7 shows the EAPE growth rate associated with the two vertical modes averaged over areas of strong CCKW activity in the Indo-Pacific warm pool (10°S – 10°N , 40°E – 180°), together with the corresponding reanalysis-produced CCKW precipitation variability. We target the Indo-Pacific warm

pool to focus on the local effect of the thermodynamic basic-state SST on CCKWs and to eliminate the modulation of CCKW events by other external factors such as midlatitude Rossby wave intrusion in the eastern Pacific and Atlantic Ocean (e.g., Straub and Kiladis 2003a; Huaman et al. 2020). The reanalysis-produced CCKW precipitation variance is positively correlated with the second mode EAPE growth rate (Fig. 7b) while being negatively correlated with the first mode EAPE growth rate (Fig. 7a).

Despite the noticeable interreanalysis differences in the sign and magnitude of the estimated EAPE growth rates, the positive relationship in Fig. 7b suggests that the CCKW precipitation variability in the reanalyses is tightly related to the representation of the second baroclinic mode EAPE growth rate. Although it should be noted that this relationship is less obvious in the interreanalysis differences in signal strength of

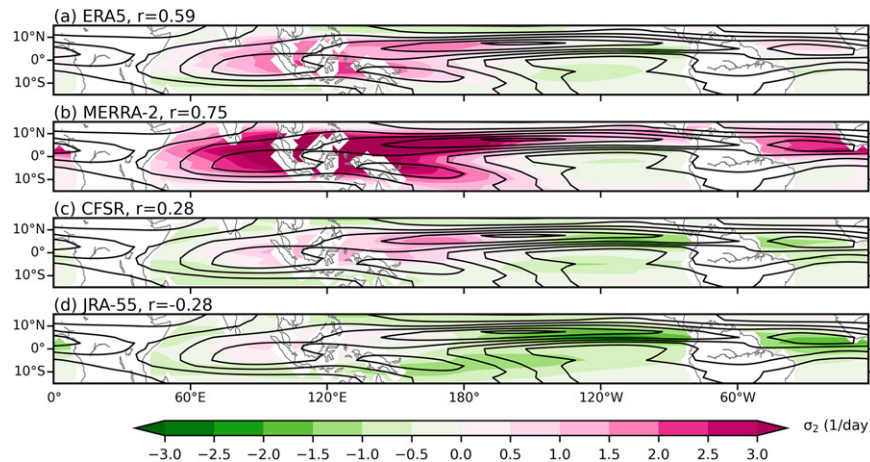


FIG. 6. As in Fig. 5, but with the EAPE growth rate of the second baroclinic mode (day^{-1} ; shading).

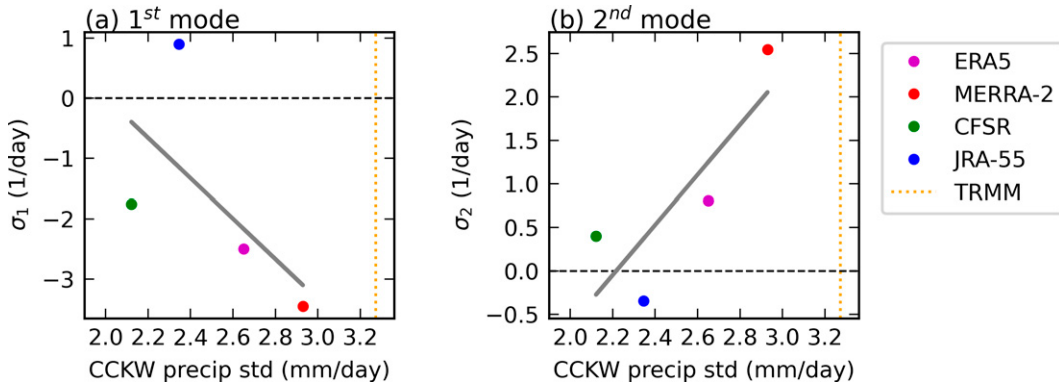


FIG. 7. Scatterplot between the standard deviation of CCKW-filtered precipitation anomalies (mm day^{-1} ; x axis) and the (a) first and (b) second baroclinic mode EAPE growth rate (day^{-1} ; y axis): purple, red, green, and blue circles indicate ERA5, MERRA-2, CFSR, and JRA-55, respectively. The gray solid line represents the linear regression line of the four dots that represent reanalysis products. Both CCKW-filtered precipitation standard deviation and the EAPE growth rate are averaged over the areas in the Indo-Pacific warm pool (10°S – 10°N , 40°E – 180° ; green box in Fig. 8), in which the reanalysis-produced CCKW precipitation standard deviation is over 1.8 mm day^{-1} . The standard deviation of CCKW-filtered precipitation variability from TRMM is marked with the vertically oriented orange dotted line.

CCKW precipitation, suggesting that the second baroclinic mode EAPE growth rate is more closely relevant to the non-normalized CCKW precipitation variability.

In response to our first research question, we show positive second baroclinic mode EAPE growth associated with both strong CCKW precipitation signal strength in the wavenumber-frequency space and strong CCKW precipitation variability over Indo-Pacific warm pool in the physical space in three reanalyses. We also show larger positive second mode EAPE growth associated with stronger reanalysis-produced CCKW precipitation. These results suggest that EAPE generation from the second mode is an important process for the growth of CCKWs.

d. Mean-state SST and the second mode CCKW EAPE growth rate

In this subsection, we investigate how the second mode EAPE growth rate changes with the basic-state SST to gain insights on how SST modulates CCKWs. Figure 8 shows the multireanalysis mean second mode EAPE growth rate together with the climatological mean SST. Given the discrepancies in the second mode EAPE growth rate among reanalysis products, we show in Fig. 8 the multireanalysis mean, which is considered as a better estimate of the real

atmosphere than each individual reanalysis product. Figure 8 shows that the second mode EAPE growth rate is positive over the Indo-Pacific and North Atlantic warm pool, collocated with the strong CCKW precipitation variability (Fig. 3a), while the second mode EAPE growth rate is negative over the eastern Pacific and South Atlantic where SST is relatively cool and CCKW precipitation variability is relatively weak (Figs. 3a and 8). The close match between the geographical variations of the second mode EAPE growth rate and that of SST implies a strong influence of the underlying SST on CCKW activity via the second mode EAPE growth rate.

We further explore the seasonal variation of the second mode EAPE growth rate, CCKW precipitation variance, and the mean-state SST in Indo-Pacific warm pool regions (Fig. 9). They appear to migrate together meridionally with the climatological seasonal cycle. The strongest CCKW precipitation variance, the largest second mode growth rate, and the warmest SST in boreal spring all locate near 5°N in ERA5, MERRA-2, and CFSR. They together reach northernmost in boreal summer and southernmost in boreal winter. The results above suggest that CCKWs are strong over the regions where the mean-state SST favors the spontaneous growth of the second mode.

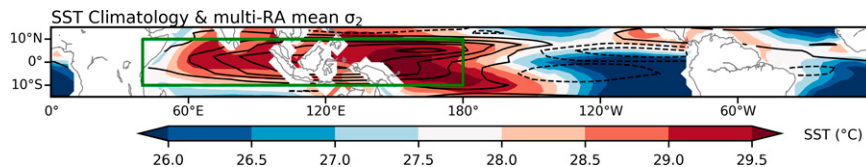


FIG. 8. The multireanalysis mean second mode EAPE growth rate (contours; day^{-1}) among four reanalyses and the climatological mean sea surface temperature ($^{\circ}\text{C}$, shading) from HadISST. The green box represents the Indo-Pacific warm pool regions (10°S – 10°N , 40°E – 180°). Contours begin at $\pm 0.5 \text{ day}^{-1}$ with an interval of 0.5 day^{-1} ; positive values are shown with solid contours and negative values with dashed contours. The zero line is omitted.

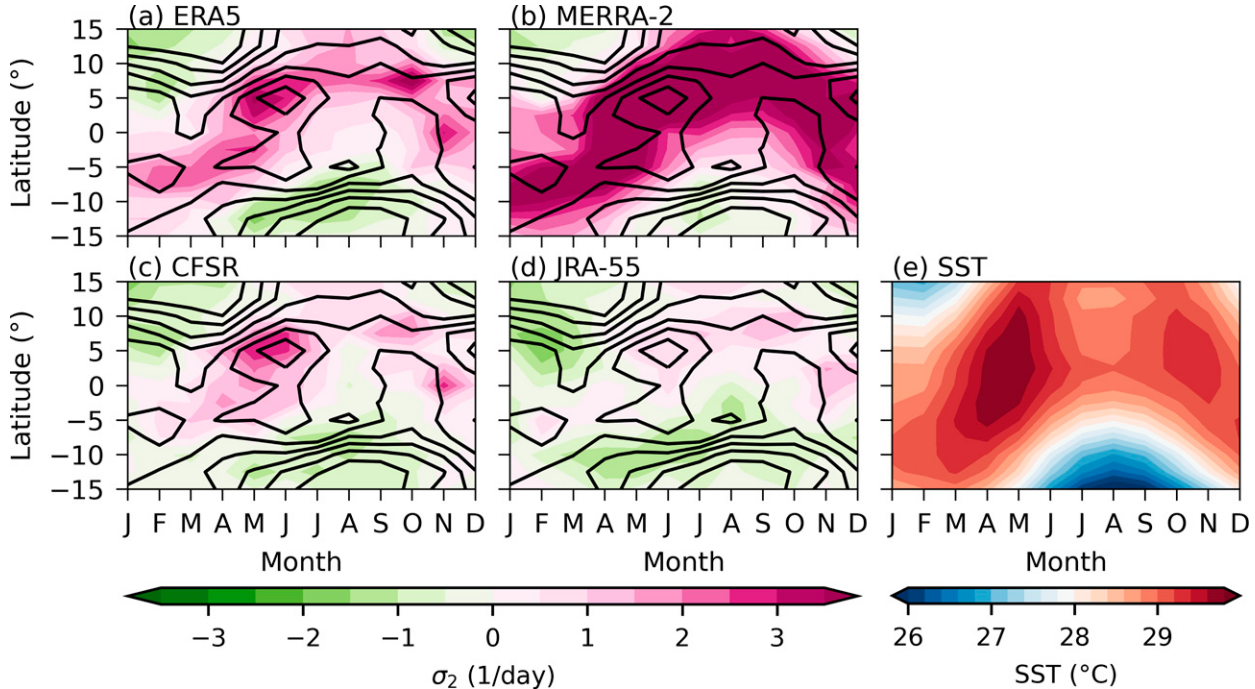


FIG. 9. The climatological seasonal cycle of zonally averaged quantities over the Indo-Pacific warm pool (40°E – 180°): (a)–(d) the standard deviation of CCKW-filtered precipitation anomalies from TRMM (mm day^{-1} ; contours) and the second mode EAPE growth rate (day^{-1} ; shading), and (e) sea surface temperature ($^{\circ}\text{C}$) from HadISST. Contours in (a)–(d) begin at 1.6 mm day^{-1} with an interval of 0.4 mm day^{-1} .

To further diagnose how the second mode EAPE growth rate changes with SST, the second mode growth rates are binned by the mean-state SST for each latitude-longitude grid for each reanalysis (Fig. 10a). In ERA5, MERRA-2, and CFSR, the second mode EAPE growth rate shows a robust positive trend with SST, especially when SST is greater than about 28°C . The rate at which the EAPE growth rate increases, however, substantially differs among reanalyses, with MERRA-2 and CFSR showing the largest and smallest trend, respectively. As in Figs. 4–6, JRA-55 shows a distinct behavior from the other reanalyses; the second mode EAPE growth rate does not show a clear increasing trend with SST.

To analyze the processes responsible for the changes of second mode EAPE growth rate associated with the mean-state SST (Fig. 10a), we decompose the second mode EAPE growth rate in Eq. (9) into three components in Eq. (15). The second mode EAPE growth rate is essentially the coefficient of the linear regression slope between the second mode diabatic heating and temperature:

$$\sigma_2 = 2 \frac{\text{cor}(\hat{Q}'_2, \hat{T}'_2)\text{std}(\hat{Q}'_2)}{\text{std}(\hat{T}'_2)}, \quad (15)$$

where $\text{cor}(\hat{Q}'_2, \hat{T}'_2)$ denotes the correlation coefficient between the second mode diabatic heating and temperature, $\text{std}(\hat{Q}'_2)$ and $\text{std}(\hat{T}'_2)$ are the standard deviations of the second mode diabatic heating and temperature anomalies, respectively. The dependence of the three components on the mean-state SST is shown in Figs. 10b–d. The increase of the second mode

EAPE growth rate with the SST in ERA5, MERRA-2, and CFSR can be explained by two following reasons: (i) the diabatic heating and temperature are more strongly correlated under high SST (Fig. 10b), and (ii) the amplitude of the diabatic heating anomalies increases with SST more dramatically than that of the temperature anomalies (Fig. 10c). Despite the robust increase of the positive second mode growth rate with SST in three reanalyses, the interreanalysis differences are shown in the magnitudes of the second mode growth rate (Fig. 10a). MERRA-2 shows the largest second mode EAPE growth rate, contributed by both the largest amplitude of the second mode diabatic heating and the most in-phase coupling between the second mode diabatic heating and temperature within CCKWs. In contrast, CFSR and JRA-55 show the smallest second mode EAPE growth rate mainly due to a weaker second mode diabatic heating and the less in-phase wave–convection coupling.

In the following we analyze how the vertical structures of CCKWs (section 2c) change with underlying mean-state SST to better understand the increase in the second mode EAPE growth rate with SST. Figure 11 shows the composite CCKW vertical structure of the zonal wind and geopotential anomalies regressed upon the CCKW precipitation time series from each reanalysis. Lag 0 denotes the day when the CCKW precipitation anomalies maximize. Negative and positive lags indicate that zonal wind or geopotential anomalies lead and lag the maximum precipitation anomalies, respectively. Considering that CCKWs propagate eastward, the x axis in Fig. 11 is flipped so that it can also be viewed as the zonal–vertical cross

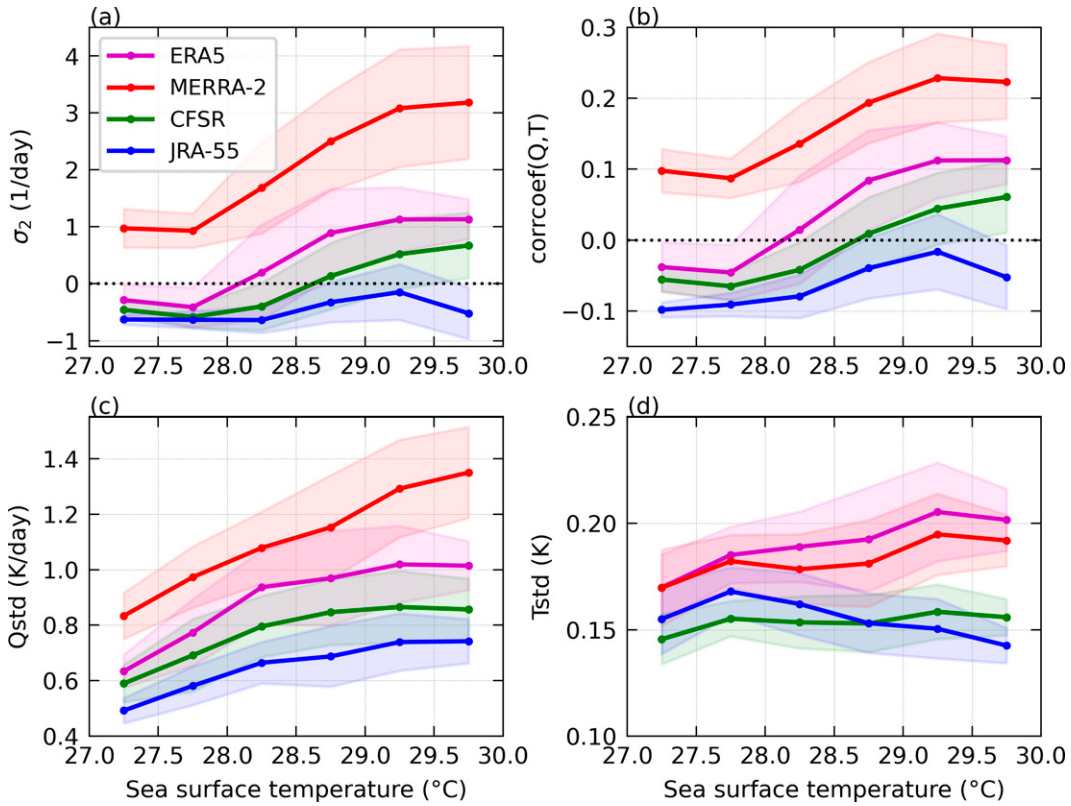


FIG. 10. (a) The second mode EAPE growth rate (day^{-1}) and (b)–(d) the three components that comprise the growth rate as a function of the climatological mean sea surface temperature ($^{\circ}\text{C}$; x axis). Purple, red, green, and blue colors indicate ERA5, MERRA-2, CFSR, and JRA-55, respectively. (b) The correlation coefficient between the CCKW-filtered second mode diabatic heating and temperature anomalies (unitless). (c) The standard deviation of the CCKW-filtered second mode diabatic heating anomalies (K day^{-1}). (d) The standard deviation of the CCKW-filtered second mode diabatic heating anomalies (K). The results are obtained from the grid points within the Indo-Pacific warm pool (10°S – 10°N , 40°E – 180°). Solid lines represent the average quantities for each SST bin and shading represents the standard deviation of the corresponding quantities for the same SST bin.

section. In all reanalyses regardless of SST values, the geopotential anomalies present extrema in the lower (below 700 hPa) and upper troposphere (above 300 hPa) for negative and positive lag days. The zonal wind anomalies are roughly in phase with the geopotential anomalies, in agreement with the dry KW theory. Around lag day 0, the zonal wind anomalies exhibit maximum convergence in the lower troposphere and maximum divergence in the upper troposphere, exhibiting the first baroclinic mode structure. On top of the first baroclinic mode structure, there appears midlevel zonal wind convergence around 500 hPa, the signature of the second baroclinic mode (e.g., Yasunaga and Mapes 2012), which is stronger over higher SST (Yang et al. 2007). The first and second mode structures in zonal wind and geopotential anomalies are reasonably represented in reanalyses compared with those from the radiosonde, though the midlevel zonal wind convergence being underestimated in reanalyses (Fig. A1 in the appendix).

Figure 12 shows the composite CCKW vertical structure of diabatic heating and temperature anomalies in ERA5. As ERA5 shows a relatively similar CCKW vertical structure to

that from the radiosonde (Fig. A1) and a realistic amplitude of CCKW precipitation variability (Fig. 3), we only show ERA5 as an example; the corresponding results for other reanalyses are shown in the supplement figures. Except for JRA-55, all other reanalyses yield similar results in vertical mode decomposition (Figs. S2–S4).

Figure 12a shows that the positive diabatic heating anomalies are westward tilted and top-heavy around lag 0, indicating the presence of both the first and second baroclinic modes (e.g., Straub and Kiladis 2003b; Yang et al. 2007; Kiladis et al. 2009; Yasunaga and Mapes 2012; Inoue et al. 2020). The midtropospheric warm and cold anomalies appear around lag days -1 and 1.5 , respectively, roughly in hydrostatic balance with the first mode geopotential anomalies. The upper-tropospheric warm anomalies near 300 hPa and the lower-tropospheric cold anomalies near 650 hPa occur around lag day 0, roughly in hydrostatic balance with the second mode geopotential anomalies in the midtroposphere around 500 hPa. The temperature anomalies within CCKWs are reasonably represented in reanalyses compared with those from the radiosonde, though the second mode warm over cold anomalies around lag day 0

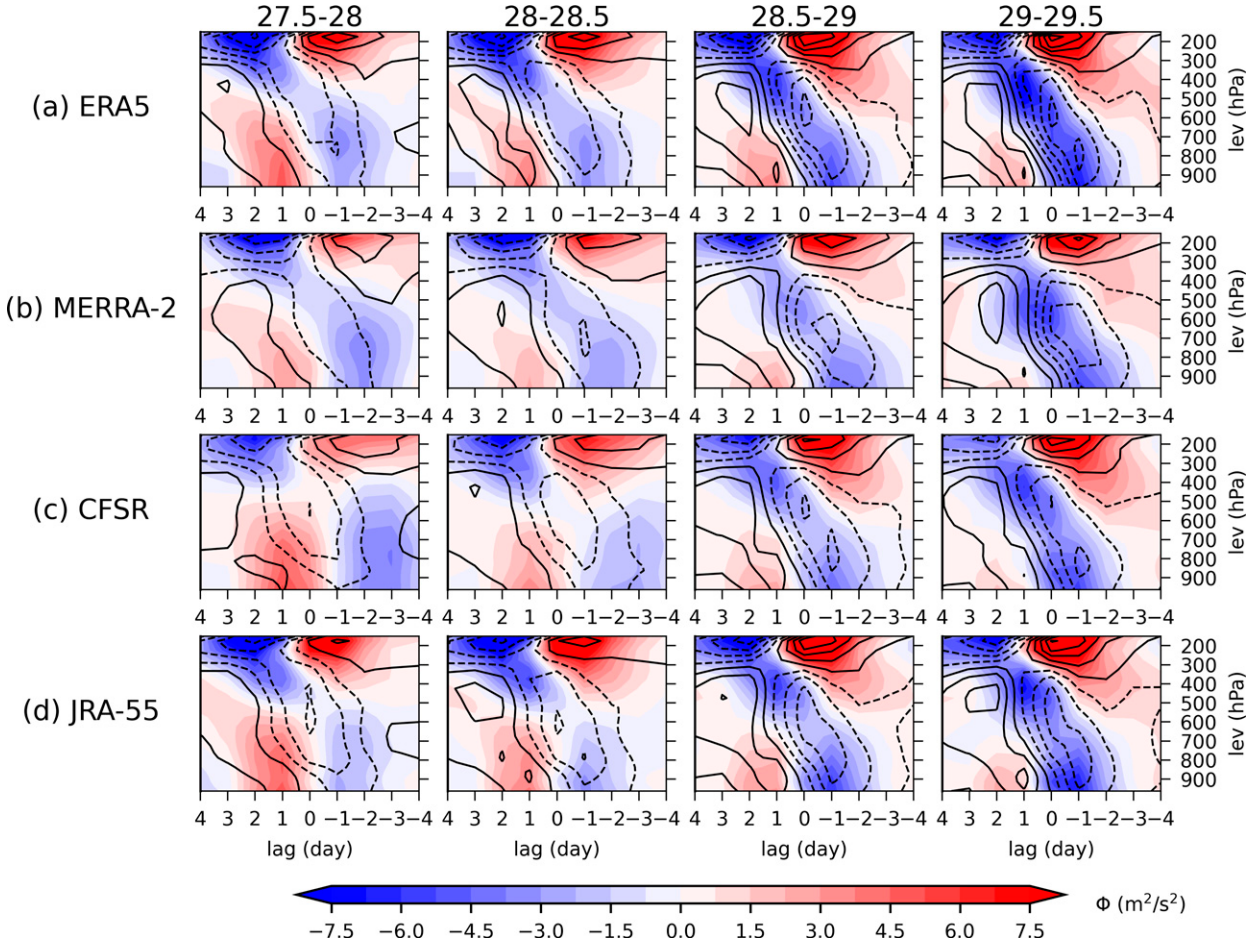


FIG. 11. Composite CCKW vertical cross section of geopotential (shading; $\text{m}^2 \text{s}^{-2}$) and zonal wind (contours; m s^{-1}) in the Indo-Pacific warm pool (10°S – 10°N , 40°E – 180°) for four climatological SST groups: (from left to right) 27.5° – 28° , 28° – 28.5° , 28.5° – 29° , and 29° – 29.5° . Each row represents each reanalysis: (a) ERA5, (b) MERRA-2, (c) CFSR, and (d) JRA-55. The composite is obtained by regressing geopotential and zonal wind anomalies upon CCKW precipitation time series from each reanalysis at each lag day at each grid point and then averaging the results over the grid point with similar climatological SST values. Negative lag days represent diabatic heating or temperature leads CCKW precipitation, and vice versa. Contours begin at $\pm 0.05 \text{ m s}^{-1}$ with an interval of 0.1 m s^{-1} . Positive and negative values are indicated by solid and dashed contours, respectively.

being underestimated, dynamically consistent with the underestimation of the second mode zonal wind (the midlevel zonal wind convergence) (Fig. A1). Under higher SST, the diabatic heating anomalies are top-heavier and the warm over cold anomalies around lag day 0 are stronger. Similar characteristics are also found in the other reanalyses (Fig. S5).

The result of extracting the first baroclinic mode component from the total anomalies (Figs. 12b,c) shows that the first baroclinic mode diabatic heating and temperature are in quadrature to near out of phase, leading to a negative first mode EAPE growth rate. The near out of phase relationship found within the first baroclinic mode component is consistent with the “soft statistical equilibrium” proposed by Emanuel et al. (1994), in which a finite convective time scale makes convection lag the forcing (vertical velocity) by a small amount, resulting in a negative correlation between diabatic heating and temperature (Emanuel et al. 1994). The amplitude of the

maximum first baroclinic mode diabatic heating on lag day 0 increases with SST by a factor of 4 from the lowest (27.5° – 28°) to highest (29° – 29.5°) SST bin.

Figures 12d and 12e show that positive second mode temperature anomalies overlap with positive diabatic heating anomalies over the regions where SST is greater than 28.5°C , resulting in a positive EAPE growth rate. While the second mode diabatic heating anomalies are substantially weaker than those of the first mode, the second mode temperature anomalies are as large as those of the first mode, consistent with the observed structure of the other convectively coupled waves in the tropics, such as the 2-day wave (Haertel et al. 2008) and WIG (Haertel and Kiladis 2004). The large second mode temperature anomalies suggest that the temperature anomalies are effectively maintained by the diabatic heating anomalies within the second baroclinic mode component.

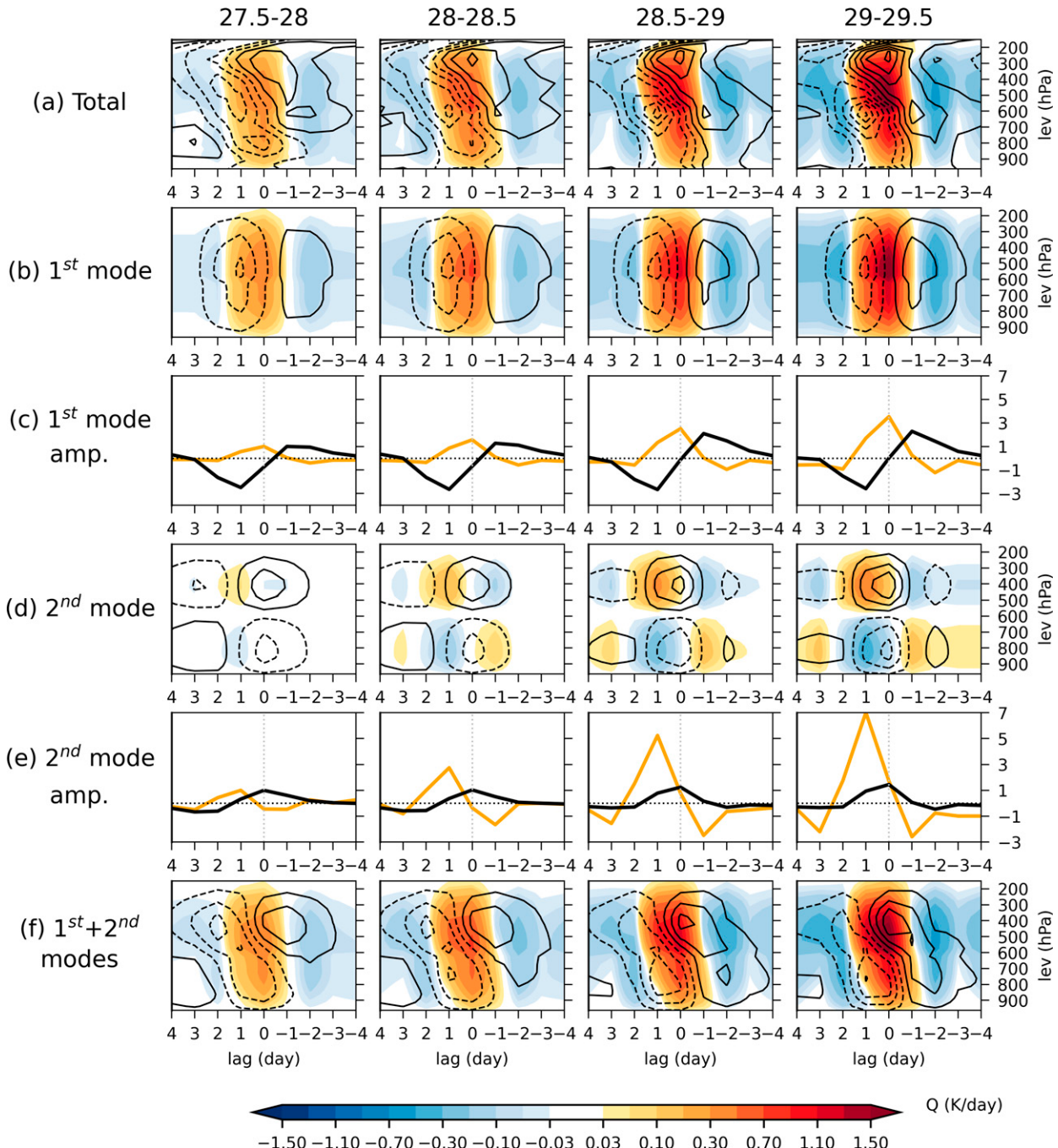


FIG. 12. (a) Composite CCKW vertical cross section of diabatic heating (K day^{-1} ; shading) and temperature (K; contours) anomalies in ERA5. (b),(d),(f) Reconstructed diabatic heating and temperature composite cross sections using (b) the first baroclinic mode component, (d) the second baroclinic mode component, and (f) the sum of the first and second mode components. Contours begin at $\pm 0.01 \text{ K}$ with an interval of 0.02 K . Positive and negative values are indicated by solid and dashed contours, respectively. (c),(e) Regression coefficients for (black) temperature and (orange) diabatic heating anomalies for the first and second baroclinic mode components. The line plots are normalized by the maximum values in SST bin of $27.5^{\circ}\text{--}28^{\circ}\text{C}$. Lag day 0 is marked in gray dotted vertical line. The corresponding results for the other reanalyses are shown in Figs. S1-3.

The empirical relationship of the second mode diabatic heating with SST shows that the maximum amplitude of the second mode diabatic heating for the highest SST bin is about 7 times greater than that for the lowest SST bin (Fig. 12e).

This rate of increase [$\sim 700\% (1.5^{\circ}\text{C})^{-1}$] is much larger than that of the maximum first mode diabatic heating amplitude [$\sim 400\% (1.5^{\circ}\text{C})^{-1}$] (Fig. 12c), indicating that the second mode diabatic heating is more sensitive to SST than the first

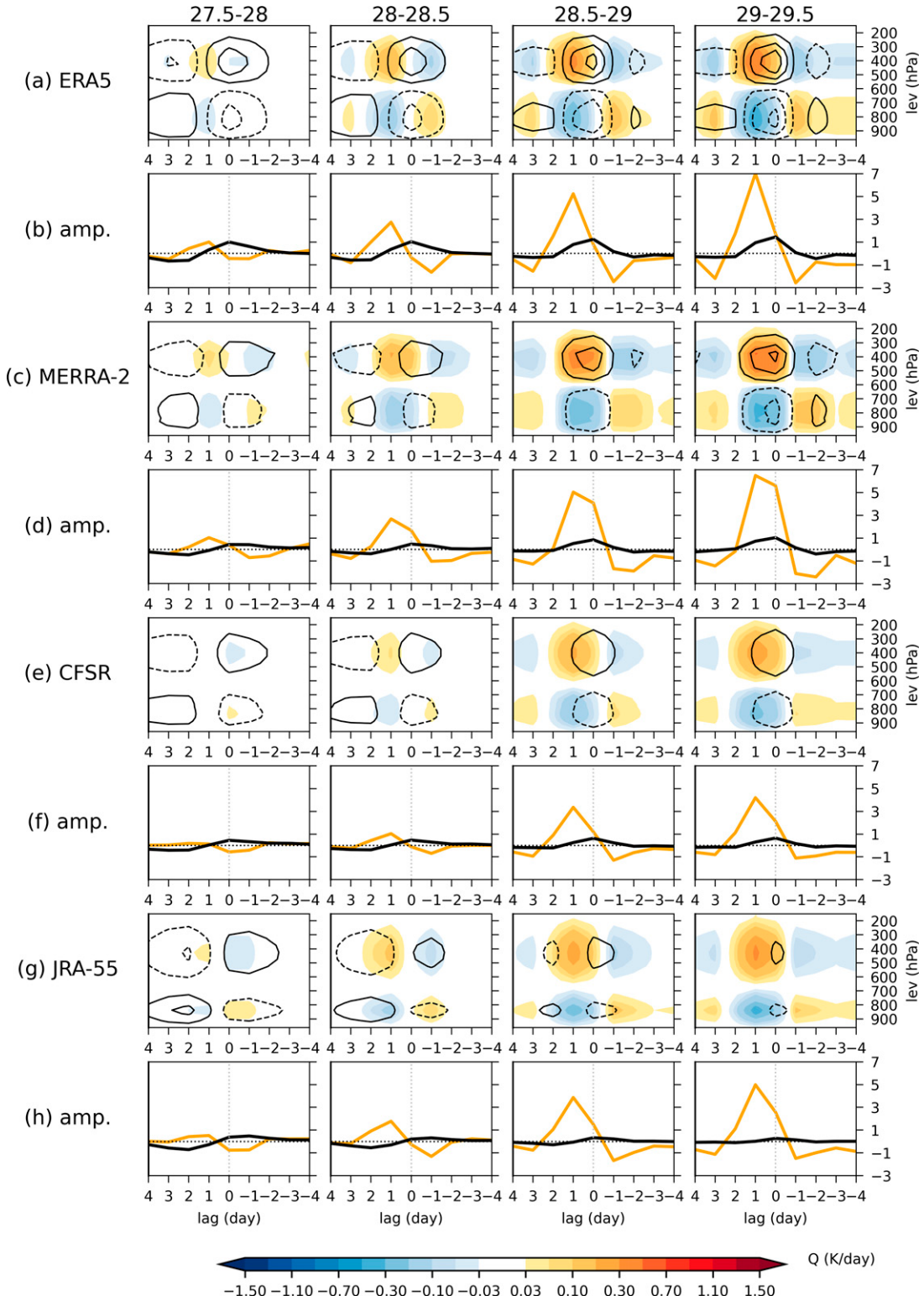


FIG. 13. Reconstructed diabatic heating and temperature composite cross sections using the second baroclinic mode component. As in Figs. 12d and 12e, but for multiple reanalyses: (a),(b) ERA5 (identical to Figs. 12d,e), (c),(d) MERRA-2, (e),(f) CFSR, and (g),(h) JRA-55. Temperature contours start from ± 0.01 K with an interval of 0.02 K; positive values are shown with solid contours and negative values are shown with dashed contours.

mode diabatic heating. Consequently, the heating is more top-heavy under high SST (Fig. 12a). On the contrary, the second mode temperature anomalies increase with SST to a much lesser degree [$\sim 150\% (1.5^{\circ}\text{C})^{-1}$] than with the first mode, qualitatively consistent with Fig. 10c.

The onset timing of the positive second mode diabatic heating anomalies also seems to change with SST. That is, the second mode diabatic heating anomalies start to become positive earlier under high SST (before lag day 0) than lower SST (after lag day 0), indicating an earlier onset of stratiform clouds. The timing of the second mode temperature peaks at the same time around lag day 0 for all SST bins. The earlier development of the positive second mode diabatic heating relative to the timing of the wave structure (the second mode temperature) produces a more in-phase relationship between the diabatic heating and temperature under high SST. However, it should be noted that the timing of the second mode diabatic heating would be more accurately diagnosed with the subdaily data than the daily data that are used in the current study.

Figure 13 compares the second mode diabatic heating and temperature anomalies associated with CCKWs among all reanalyses. MERRA-2 and CFSR show features that are consistent with those from ERA5: under high SST, the second mode diabatic heating is much stronger and the convection and wave are more tightly coupled. The higher sensitivity of the second mode diabatic heating with the SST, as well as the more in-phase relationship between diabatic heating and temperature under high SST, explains why the second mode EAPE growth rate increases with SST in ERA5, MERRA-2, and CFSR, though with significant interreanalysis differences.

The steep increase in the second mode diabatic heating with SST is likely due to the combined effect of that the production of stratiform clouds is stronger as the stronger deep convection detains more hydrometers to the surrounding and that the maintenance of those hydrometers is easier as the environment is more humid over higher SST. While the former factor is suggested in Fig. 12b, the second part is supported by Ahmed and Schumacher (2015), who showed that the moisture sensitivity of stratiform rain increases with the degree of environmental saturation. Figure 14 shows that, as expected, the mean-state SST is almost linearly correlated with the mean-state column relative humidity (CRH), consistent with the weak second mode diabatic heating anomalies when SST is lower than 28°C ($\text{CRH} < 65\%$). Figure 15 shows the composite CCKW vertical structure of moisture anomalies (shading) and the second mode diabatic heating anomalies (magenta contours). In each reanalysis for all SST bins, pronounced positive moisture anomalies appear on lag day 0 in around 800 hPa (700 hPa in CFSR). For high SST bins, the low-tropospheric moisture anomalies are followed by positive moisture anomalies in around 600-hPa on lag day 1. It seems from Fig. 15 that the second mode diabatic heating anomalies develop only when the midlevel moisture anomalies are sufficiently large, suggesting that the midlevel moisture anomalies regulate stratiform heating (Kuang 2008). Interestingly, for the highest two SST bins, the amplitude of CCKW moisture perturbations is similar while the second mode diabatic heating is much stronger over higher mean-state SST, which is

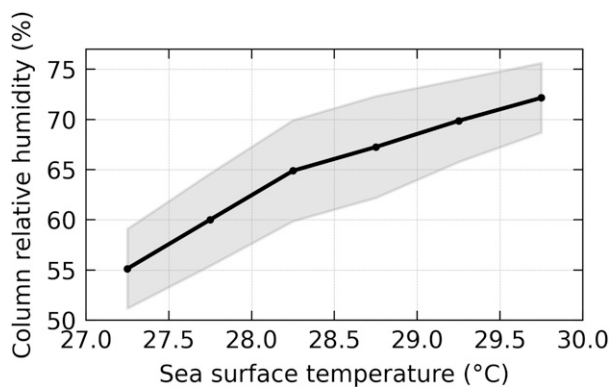


FIG. 14. Mean-state column relative humidity averaged over four reanalysis products composited based on the climatological mean-state sea surface temperature from HadISST in Indo-Pacific warm pool (10°S – 10°N , 40°E – 180°).

consistent with the notion that the same moisture perturbation would produce a larger stratiform precipitation increase under a higher environmental CRH (Ahmed and Schumacher 2015). We hypothesize that under high mean-state SST (CRH), water vapor and hydrometeors detrained from deep cumulus clouds in the upper troposphere can more easily form and prolong, helping the stratiform clouds sustain longer. Despite the robust increase of the positive second mode growth rate with SST in three reanalyses, considerable interreanalysis discrepancies in CCKW vertical structure in the thermodynamic field are observed (Figs. 13, 15 and Fig. S4). Consistent with the underestimation of the temperature and zonal wind anomalies within the second baroclinic mode in reanalyses, the midtropospheric moisture anomalies are also underestimated in reanalyses compared with that from the radiosonde (Fig. A1). Our results suggest that improving the representation of the stratiform cloud processes is key to a realistic representation of CCKWs in reanalyses.

4. Summary and conclusions

In this study, we examined the precipitation variability, vertical structure, and energetics of the convectively coupled Kelvin waves (CCKWs) in four modern reanalysis products: ERA5, MERRA-2, CFSR, and JRA-55. The vertical structure of the first two baroclinic modes for temperature and diabatic heating was obtained empirically as the two leading EOFs of diabatic heating anomalies in each reanalysis. For each vertical mode, the eddy available potential energy (EAPE) growth rate—the normalized covariance between temperature and diabatic heating—was calculated in the wavenumber-frequency and physical domain as a proxy for the growth rate of CCKWs due to EAPE production. The relationship between CCKW precipitation variability and the EAPE growth rate from the first and second baroclinic modes was examined in the context of the geographical and seasonal variations to assess the relative importance of the first and second baroclinic modes in CCKW maintenance. The vertical structure of the diabatic heating, temperature, and moisture

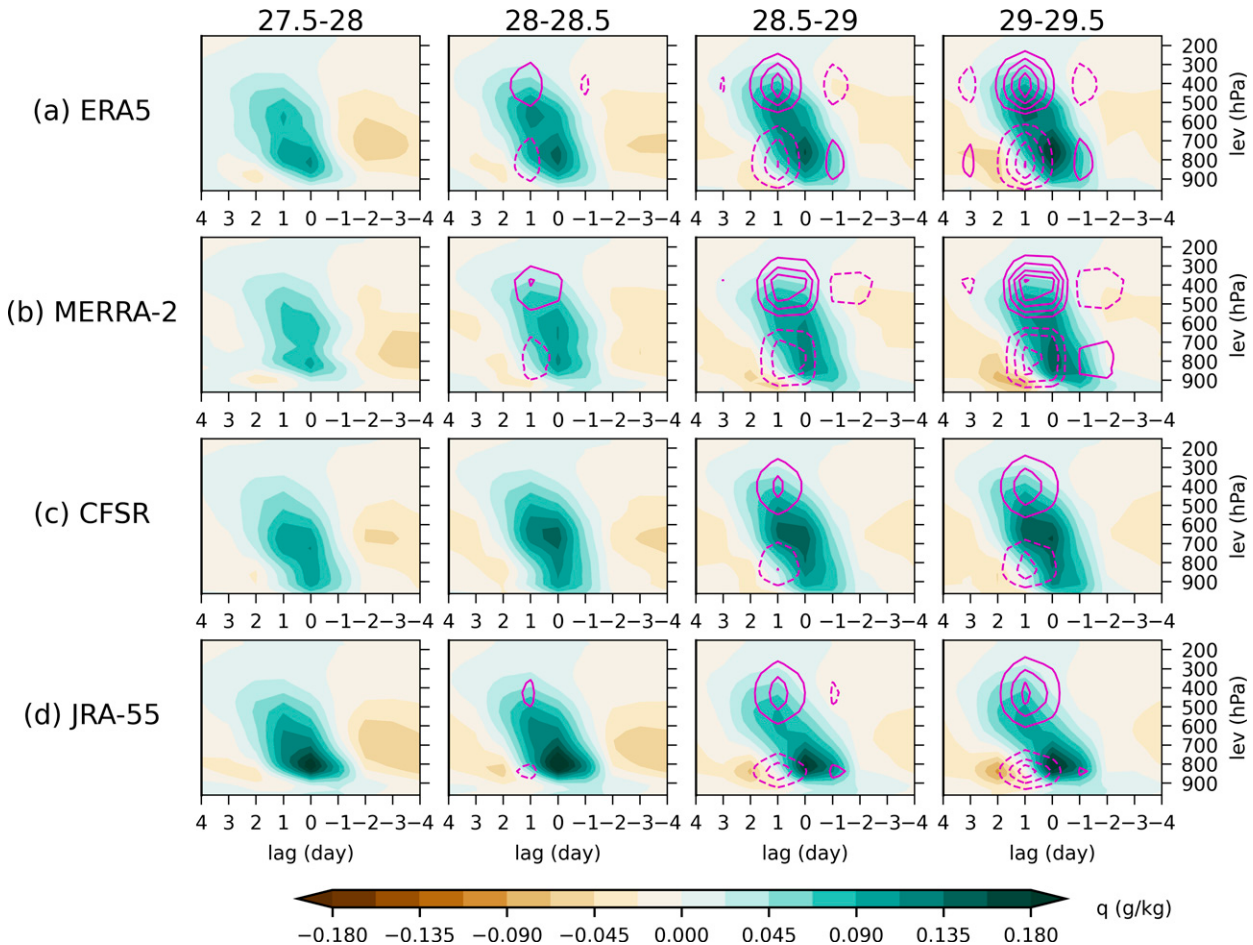


FIG. 15. As in Fig. 11, but for specific humidity (g kg^{-1} ; shading) and the second mode diabatic heating (K day^{-1} ; contours). Contours begin at $\pm 0.1 \text{ K day}^{-1}$, with an interval of 0.1 K day^{-1} .

anomalies within CCKWs was compared between different mean-state sea surface temperature (SST) conditions to understand how the underlying SST affects the EAPE growth rate, and hence CCKWs.

Below we present a summary of the main results in the form of answering the three research questions raised in section 1.

- 1) Are CCKWs destabilized within the first or second baroclinic mode component?

In three out of the four RAs, our diagnosis of the CCKW energetics showed that the EAPE grows within the second baroclinic mode while being damped within the first baroclinic mode in a time-mean composite sense. The second mode EAPE growth rate was found to be positive in the spectral band of pronounced CCKW signal strength in the wavenumber-frequency space and in the areas of strong CCKW precipitation variability in the latitude-longitude domain. Our results strongly suggest that CCKWs are destabilized within the second baroclinic mode, which is therefore key to understanding the geographical and seasonal variation, and also the scale selection of CCKWs.

2) How are CCKWs modulated by the mean-state SST?

We showed that the second mode EAPE growth rate increases with the mean-state SST, again in three out of the four reanalyses. The increase in the second mode EAPE growth rate with SST was found to be due to increases in the magnitude of the second mode diabatic heating and the correlation between the second mode diabatic heating and temperature anomalies. Based on the observation that high mean-state SST corresponds to high mean-state CRH, it was hypothesized that under high mean-state SST, water vapor and hydrometeors detrained from deep cumulus clouds in the upper troposphere can more easily form and prolong, which then help stratiform clouds sustain longer. Our results suggest that stratiform cloud formation and maintenance, which is an important process for the growth of CCKWs, is highly dependent on the mean-state SST, though more work is needed to fully understand the relationship between SST and CCKW precipitation variability.

- 3) How well do modern reanalysis products represent the CCKWs?

In terms of CCKW precipitation variability, all reanalyses exhibited realistic representation of CCKW precipitation

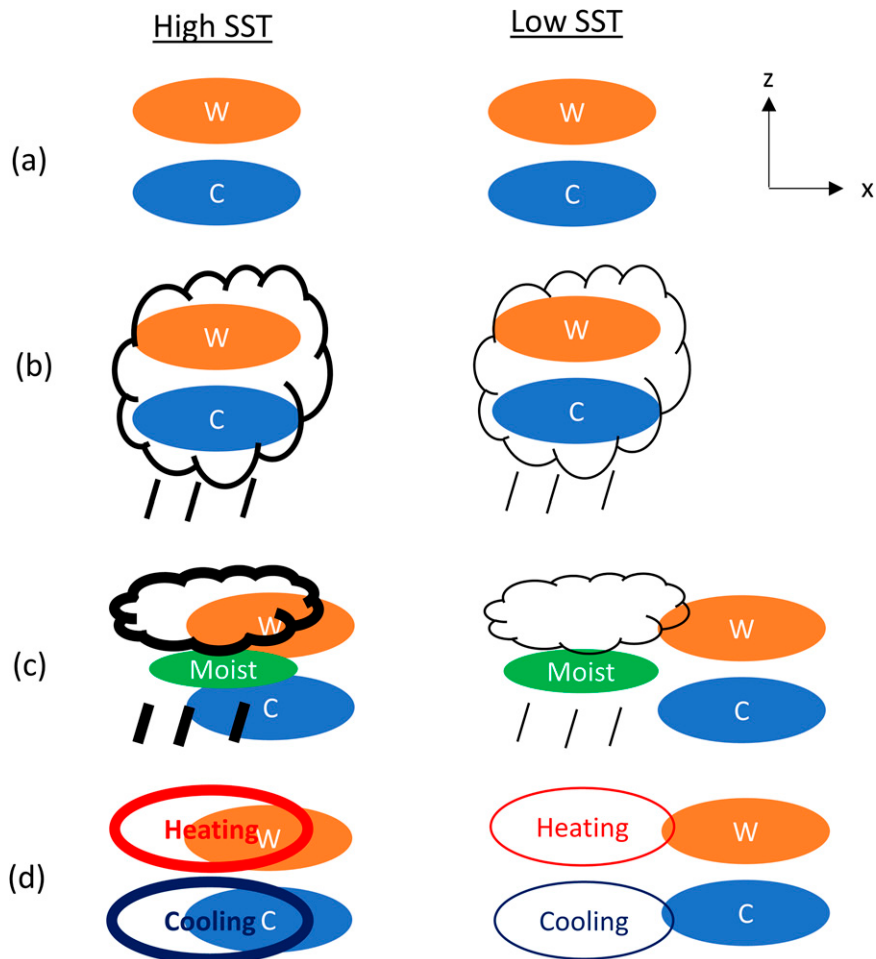


FIG. 16. Schematic diagram of the effect of mean SST on how CCKWs are destabilized within the second baroclinic component. (a) An initial second mode temperature perturbation with warm anomaly aloft and cold anomaly below. (b) The cold anomaly below reduces convective inhibition (CIN) and triggers deep convection. (c) Deep convection moistens the midtroposphere with a lag time that is longer under (left) low SST than (right) high SST. Stratiform cloud develops above the positive midtropospheric moisture anomaly and produces stratiform rain beneath, which creates the heating over cooling structure. Meanwhile, the wave—the second mode temperature anomaly—propagates eastward. (d) (left) Under high SST, with stratiform heating and cooling overlapping with the original temperature perturbation, CCKWs can grow and maintain. (right) Under low SST, however, CCKW growth is not supported as the stratiform heating and cooling not overlap with the original temperature perturbation with a longer lag time in (c).

signal strength in the wavenumber–frequency domain. The geographical distribution of CCKW amplitude measured by the standard deviation of precipitation variability are also reasonably represented, though the amplitude is commonly underestimated. Regarding the first and second mode EAPE growth rates, however, considerable interreanalysis discrepancies were found, highlighting the discrepancies associated with convection and cloud processes between reanalysis products. Additionally, the dependency of the second mode growth rate on the basic-state SST also differs largely in different reanalyses. The difference in the magnitude of second mode diabatic heating and temperature anomalies

appeared to be mainly responsible for the interreanalysis differences in the second mode EAPE growth rate and its sensitivity to SST.

Collectively, our results highlighted the importance of the second baroclinic mode and related thermodynamic processes, especially stratiform clouds, in the maintenance of CCKWs in reanalyses. We argue based on the results that improving the representation of stratiform clouds is key to a realistic representation of CCKWs in reanalyses. Our results are also supportive of the simple models for CCKWs in which CCKWs are destabilized within the second baroclinic mode.

The destabilization processes that our results suggest are consistent with the hypothesis proposed in the simple model of Kuang (2008), with addition of the role of mean-state SST emphasized in this study. Incorporating our findings and the linear perturbation theory, which explains how a given wave perturbations of a small amplitude grow and propagate in simple models of CCKWs (e.g., Mapes 2000; Kuang 2008), we present the hypothetical processes by which CCKWs are destabilized within the second mode component under high SST basic state in Fig. 16.

Assuming there is a randomly perturbed temperature field containing the second baroclinic mode structure (Fig. 16a), Fig. 16 describes the processes by which the second baroclinic mode component is amplified. The processes are as follows. The low-level cold anomalies reduce the convective inhibition (CIN) which triggers the deep convection (Mapes 2000) (Fig. 16b). The deep convection then moistens the column at the original location. As the wave propagates eastward, the resulting midlevel moisture anomalies trail the wave (Fig. 16c). The moisture anomaly provides a favorable condition for deep convection to grow above the melting level, which leads to stratiform heating trailing the deep cumulus clouds (Fig. 16c). As a result, the second mode warm over cold temperature (the wave structure) is positively correlated with the stratiform heating and thus being amplified (Fig. 16d). This positive feedback loop describes how CCKWs are destabilized within the second baroclinic mode under the moisture-stratiform instability (Kuang 2008). However, the above positive feedback loop is switched on only when the mean-state SST is high enough. Under low SST, with the same warm over cold anomalies in the first place (Fig. 16a), the stratiform heating occurs later and with a weaker amplitude, possibly because it takes a longer time for the midtroposphere to be moistened to the extent that supports the development of stratiform (Fig. 16c). Consequently, the heating over cooling from the stratiform does not overlap with the initial warm over cold anomalies, and the wave cannot be amplified (Fig. 16d).

It should be noted that while our study argued the internal convection-wave feedback via EAPE generation is an important process governing the spontaneous growth of CCKWs, other processes may also affect the growth of CCKWs. For example, CCKWs may also grow by the external midlatitude forcing which generates eddy kinetic energy (EKE), especially in the eastern Pacific and the Atlantic Ocean (Tulich and Kiladis 2021). Further examination of the extent to which CCKW variability is associated with the internal dynamics (i.e., EAPE growth) and the external forcing is warranted.

While our study proposed a potential mechanism of how SST modulates CCKWs via the stratiform processes, the individual steps we proposed, from the mean-state SST, to the moisture-precipitation relationship, and to stratiform processes within CCKWs, should be further investigated and validated in future studies. Although SST is an important basic-state quantity that shows robust relationship with CCKW activity, other basic-state variables (i.e., zonal wind) may also affect CCKWs (Tulich and Kiladis 2021). Future studies should further examine the relationship between CCKWs and other basic-state variables.

Last, the diagnostic framework developed in this study can be applied to global climate model (GCM) simulations of the current and future climates to understand intermodel differences in the representation of CCKWs and the model-simulated changes in CCKW characteristics in a warmer climate. Such modeling studies would help improve the representation of CCKWs in GCMs and reduce the uncertainty associated with future projection of CCKWs and their associated precipitation variability.

Acknowledgments. We appreciated the three anonymous reviewers for their constructive comments on the earlier version of the manuscript. This research was supported by the NASA MAPP program (80NSSC17K0227), NOAA CVP program (NA18OAR4310300), DOE RGMA program (DE-SC0016223), and KMA R&D program (KMI2021-01210).

Data availability statement. All data used for analysis are available online via the following links:

- ERA5: <https://www.ecmwf.int/en/forecasts/dataset/ecmwf-reanalysis-v5>,
- MERRA-2: <https://disc.gsfc.nasa.gov/datasets?project=MERRA-2>,
- CFSR: <https://rda.ucar.edu/datasets/ds094.0/>,
- JRA-55: <https://rda.ucar.edu/datasets/ds628.0/>,
- HadISST: <https://rda.ucar.edu/datasets/ds277.3/>,
- TRMM: https://disc.gsfc.nasa.gov/datasets/TRMM_3B42_Daily_7/ summary, and
- IGRA: <https://www.ncei.noaa.gov/products/weather-balloon/integrated-global-radiosonde-archive>.

APPENDIX

Intercomparison of CCKW Vertical Structures in Reanalyses and the Radiosonde in Majuro

To aid the interpretation of the interreanalysis differences in the results presented in the previous sections, we evaluate the vertical structure of the CCKWs from reanalyses against that from the radiosonde observations in Majuro. The zonal wind, geopotential, temperature, and moisture anomalies associated with CCKWs that developed in Majuro are shown in Fig. A1. The first baroclinic mode structure—the midtropospheric temperature peak, the upper-level zonal wind divergence and lower-level zonal wind convergence—is similar across the reanalyses. On the other hand, the second baroclinic mode structure—the warm over cold anomalies, the midtropospheric zonal wind convergence, and the midtropospheric moisture anomalies between lag day 0 and 1—is underestimated in reanalyses and presents pronounce discrepancies among reanalyses. In particular, temperature presents an eastward-tilted structure in below 700-hPa in JRA-55 (Fig. A1e). This leads to the temperature anomalies and the diabatic heating anomalies being less in phase for the second mode and more in phase for the first mode. We speculate that the peculiar temperature structure in JRA-55 is why it shows the energetics results that are opposite to those from the other reanalyses (Fig. S4). While CFSR shows a slight eastward tilting in low levels, ERA5, MERRA-2, and the radiosonde observations do not show an

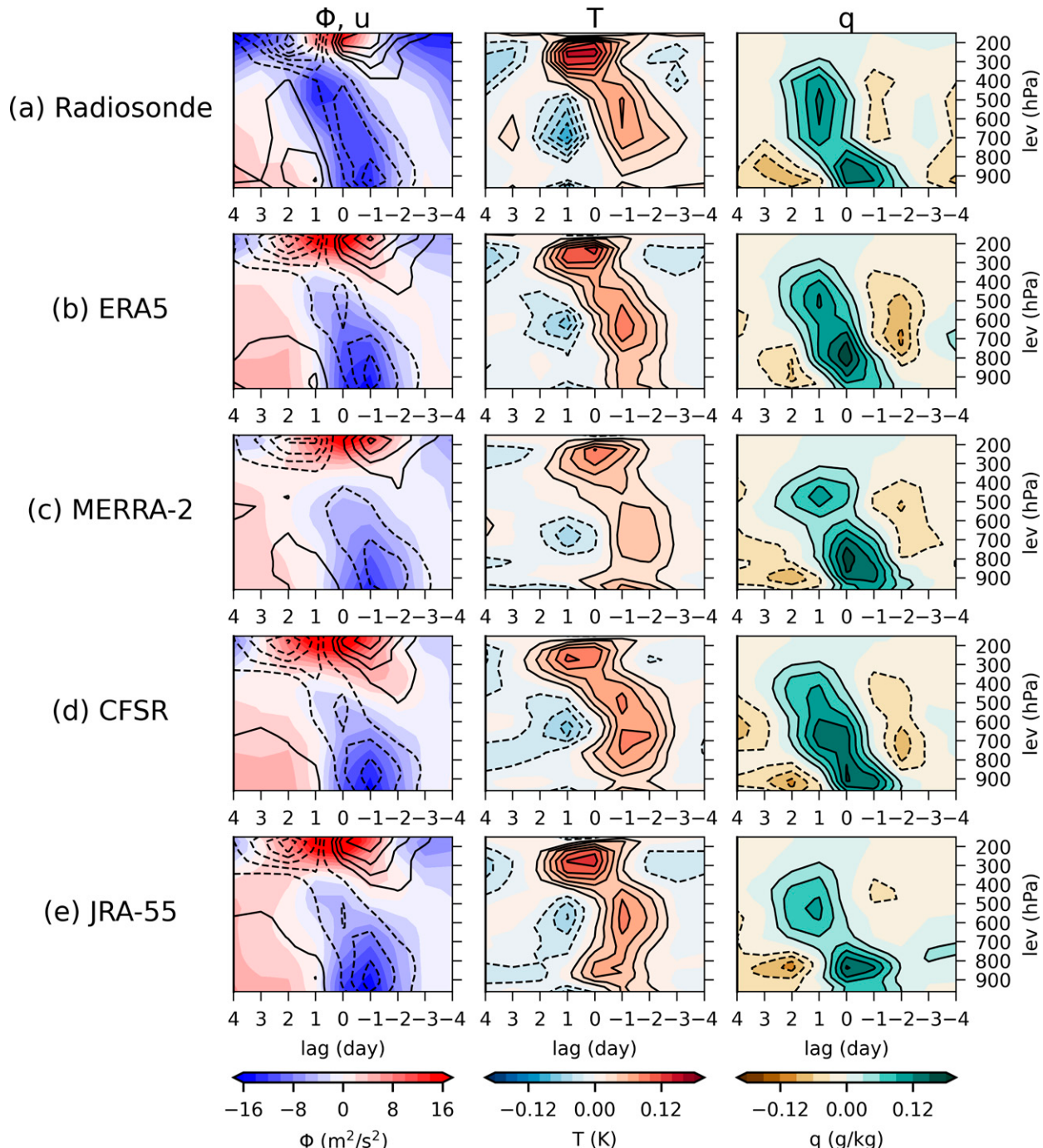


FIG. A1. Composite CCKW vertical cross section of (left) geopotential ($\text{m}^2 \text{s}^{-2}$; shading), (center) zonal wind (m s^{-1} ; shading), (right) temperature (K; shading), and (right) specific humidity (g kg^{-1} ; shading) from (a) radiosonde and each reanalysis product: (b) ERA5, (c) MERRA-2, (d) CFSR, and (e) JRA-55. (a) The composite cross sections are obtained from the radiosonde data in Majuro ($7.0683^\circ\text{N}, 171.2942^\circ\text{E}$). Each field is regressed upon CCKW-filtered precipitation from TRMM at different lag days. (b)–(e) A nearest grid point and CCKW-filtered precipitation from each reanalysis are used for the reanalysis composite results. For the left panel, zonal wind contours begin at $\pm 0.15 \text{ m s}^{-1}$ with an interval of 0.15 m s^{-1} ; positive values are shown with solid contours and negative values are shown with dashed contours.

eastward-tilting structure, consistent with past studies (e.g., Straub and Kiladis 2003b; Kiladis et al. 2009). It should be noted that there are two caveats in this comparison. First, we use the 2.5° regredded data for comparison, which involves some smoothing that may reduce the interreanalysis differences and biases. Second, since Majuro sonde data are assimilated in all four reanalysis products, each reanalysis data are forced to converge to the Majuro sonde data. Therefore, the comparison between each reanalysis and the radiosonde data at Majuro can serve as the lower bound of the interreanalysis differences and biases.

REFERENCES

- Adames, Á. F., and J. M. Wallace, 2014: Three-dimensional structure and evolution of the vertical velocity and divergence fields in the MJO. *J. Atmos. Sci.*, **71**, 4661–4681, <https://doi.org/10.1175/JAS-D-14-0091.1>.
- Ahmed, F., and C. Schumacher, 2015: Convective and stratiform components of the precipitation-moisture relationship. *Geophys. Res. Lett.*, **42**, 10453–10462, <https://doi.org/10.1002/2015GL066957>.
- Benedict, J. J., E. D. Maloney, A. H. Sobel, D. M. Frierson, and L. J. Donner, 2013: Tropical intraseasonal variability in version 3 of the GFDL atmosphere model. *J. Climate*, **26**, 426–449, <https://doi.org/10.1175/JCLI-D-12-00103.1>.
- Bessafi, M., and M. C. Wheeler, 2006: Modulation of south Indian Ocean tropical cyclones by the Madden-Julian oscillation and convectively coupled equatorial waves. *Mon. Wea. Rev.*, **134**, 638–656, <https://doi.org/10.1175/MWR3087.1>.
- Chen, B., W.-w. Tung, and M. Yanai, 2016: Multiscale temporal mean features of perturbation kinetic energy and its budget in the tropics: Review and computation. *Multiscale Convection-Coupled Systems in the Tropics: A Tribute to Dr. Michio Yanai*, Meteor. Monogr., No. 56, Amer. Meteor. Soc., <https://doi.org/10.1175/AMSMONOGRAPH-D-15-0017.1>.
- Durre, I., R. S. Vose, and D. B. Wuertz, 2006: Overview of the Integrated Global Radiosonde Archive. *J. Climate*, **19**, 53–68, <https://doi.org/10.1175/JCLI3594.1>.
- Emanuel, K. A., 1987: An air-sea interaction model of intraseasonal oscillations in the tropics. *J. Atmos. Sci.*, **44**, 2324–2340, [https://doi.org/10.1175/1520-0469\(1987\)044<2324:AASIMO>2.0.CO;2](https://doi.org/10.1175/1520-0469(1987)044<2324:AASIMO>2.0.CO;2).
- , J. D. Neelin, and C. S. Bretherton, 1994: On large-scale circulations in convecting atmospheres. *Quart. J. Roy. Meteor. Soc.*, **120**, 1111–1143, <https://doi.org/10.1002/qj.49712051902>.
- Flatau, M. K., P. J. Flatau, J. Schmidt, and G. N. Kiladis, 2003: Delayed onset of the 2002 Indian monsoon. *Geophys. Res. Lett.*, **30**, 1768, <https://doi.org/10.1029/2003GL017434>.
- Fulton, S. R., and W. H. Schubert, 1985: Vertical normal mode transforms: Theory and application. *Mon. Wea. Rev.*, **113**, 647–658, [https://doi.org/10.1175/1520-0493\(1985\)113<0647:VNMTTA>2.0.CO;2](https://doi.org/10.1175/1520-0493(1985)113<0647:VNMTTA>2.0.CO;2).
- Gelaro, R., and Coauthors, 2017: The Modern-Era Retrospective Analysis for Research and Applications, version 2 (MERRA-2). *J. Climate*, **30**, 5419–5454, <https://doi.org/10.1175/JCLI-D-16-0758.1>.
- Haertel, P. T., and G. N. Kiladis, 2004: Dynamics of 2-day equatorial waves. *J. Atmos. Sci.*, **61**, 2707–2721, <https://doi.org/10.1175/JAS3352.1>.
- , —, A. Denno, and T. M. Rickenbach, 2008: Vertical-mode decompositions of 2-day waves and the Madden-Julian oscillation. *J. Atmos. Sci.*, **65**, 813–833, <https://doi.org/10.1175/2007JAS2314.1>.
- Hersbach, H., and Coauthors, 2020: The ERA5 global reanalysis. *Quart. J. Roy. Meteor. Soc.*, **146**, 1999–2049, <https://doi.org/10.1002/qj.3803>.
- Huaman, L., C. Schumacher, and G. N. Kiladis, 2020: Eastward-propagating disturbances in the tropical Pacific. *Mon. Wea. Rev.*, **148**, 3713–3728, <https://doi.org/10.1175/MWR-D-20-0029.1>.
- Huffman, G. J., and Coauthors, 2007: The TRMM Multisatellite Precipitation Analysis (TMPA): Quasi-global, multiyear, combined-sensor precipitation estimates at fine scales. *J. Hydrometeor.*, **8**, 38–55, <https://doi.org/10.1175/JHM560.1>.
- Hung, M.-P., J.-L. Lin, W. Wang, D. Kim, T. Shinoda, and S. J. Weaver, 2013: MJO and convectively coupled equatorial waves simulated by CMIP5 climate models. *J. Climate*, **26**, 6185–6214, <https://doi.org/10.1175/JCLI-D-12-00541.1>.
- Inoue, K., Á. F. Adames, and K. Yasunaga, 2020: Vertical velocity profiles in convectively coupled equatorial waves and MJO: New diagnoses of vertical velocity profiles in the wavenumber-frequency domain. *J. Atmos. Sci.*, **77**, 2139–2162, <https://doi.org/10.1175/JAS-D-19-0209.1>.
- Khouider, B., and A. J. Majda, 2006: A simple multicloud parameterization for convectively coupled tropical waves. Part I: Linear analysis. *J. Atmos. Sci.*, **63**, 1308–1323, <https://doi.org/10.1175/JAS3677.1>.
- Kiladis, G. N., M. C. Wheeler, P. T. Haertel, K. H. Straub, and P. E. Roundy, 2009: Convectively coupled equatorial waves. *Rev. Geophys.*, **47**, RG2003, <https://doi.org/10.1029/2008RG000266>.
- Kim, D., M. I. Lee, D. Kim, S. D. Schubert, D. E. Waliser, and B. Tian, 2014: Representation of tropical subseasonal variability of precipitation in global reanalyses. *Climate Dyn.*, **43**, 517–534, <https://doi.org/10.1007/s00382-013-1890-x>.
- Kobayashi, S., and Coauthors, 2015: The JRA-55 reanalysis: General specifications and basic characteristics. *J. Meteor. Soc. Japan*, **93**, 5–48, <https://doi.org/10.2151/jmsj.2015-001>.
- Kuang, Z., 2008: A moisture-stratiform instability for convectively coupled waves. *J. Atmos. Sci.*, **65**, 834–854, <https://doi.org/10.1175/2007JAS2444.1>.
- Latos, B., and Coauthors, 2021: Equatorial waves triggering extreme rainfall and floods in southwest Sulawesi, Indonesia. *Mon. Wea. Rev.*, **149**, 1381–1401, <https://doi.org/10.1175/MWR-D-20-0262.1>.
- Liebmann, B., G. N. Kiladis, L. M. Carvalho, C. Jones, C. S. Vera, I. Bladé, and D. Allured, 2009: Origin of convectively coupled Kelvin waves over South America. *J. Climate*, **22**, 300–315, <https://doi.org/10.1175/2008JCLI2340.1>.
- Ling, J., and C. Zhang, 2013: Diabatic heating profiles in recent global reanalyses. *J. Climate*, **26**, 3307–3325, <https://doi.org/10.1175/JCLI-D-12-00384.1>.
- Lin, J.-L., and Coauthors, 2006: Tropical intraseasonal variability in 14 IPCC AR4 climate models. Part I: Convective signals. *J. Climate*, **19**, 2665–2690, <https://doi.org/10.1175/JCLI3735.1>.
- Lindzen, R. S., 1974: Wave-CISK in the tropics. *J. Atmos. Sci.*, **31**, 156–179, [https://doi.org/10.1175/1520-0469\(1974\)031<0156:WCITT>2.0.CO;2](https://doi.org/10.1175/1520-0469(1974)031<0156:WCITT>2.0.CO;2).
- Long, C. S., M. Fujiwara, S. Davis, D. M. Mitchell, and C. J. Wright, 2017: Climatology and interannual variability of dynamic variables in multiple reanalyses evaluated by the SPARC Reanalysis Intercomparison Project (S-RIP). *Atmos. Chem. Phys.*, **17**, 14 593–14 629, <https://doi.org/10.5194/acp-17-14593-2017>.

- Lorenz, E. N., 1955: Available potential energy and the maintenance of the general circulation. *Tellus*, **7**, 157–167, <https://doi.org/10.3402/tellusa.v7i2.8796>.
- Mapes, B. E., 2000: Convective inhibition, subgrid-scale triggering energy, and stratiform instability in a toy tropical wave model. *J. Atmos. Sci.*, **57**, 1515–1535, [https://doi.org/10.1175/1520-0469\(2000\)057<1515:CISSTE>2.0.CO;2](https://doi.org/10.1175/1520-0469(2000)057<1515:CISSTE>2.0.CO;2).
- Masunaga, H., 2007: Seasonality and regionality of the Madden-Julian oscillation, Kelvin wave, and equatorial Rossby wave. *J. Atmos. Sci.*, **64**, 4400–4416, <https://doi.org/10.1175/2007JAS2179.1>.
- Matsuno, T., 1966: Quasi-geostrophic motions in the equatorial area. *J. Meteor. Soc. Japan*, **44**, 25–43, https://doi.org/10.2151/jmsj1965.44.1_25.
- Mekonnen, A., C. D. Thorncroft, A. R. Aiyyer, and G. N. Kiladis, 2008: Convectively coupled Kelvin waves over tropical Africa during the boreal summer: Structure and variability. *J. Climate*, **21**, 6649–6667, <https://doi.org/10.1175/2008JCLI2008.1>.
- Murata, F., M. D. Yamanaka, H. Hashiguchi, S. Mori, M. Kudsy, T. Sribimawati, B. Suhardi, and Emrizal, 2006: Dry intrusions following eastward-propagating synoptic-scale cloud systems over Sumatera Island. *J. Meteor. Soc. Japan*, **84**, 277–294, <https://doi.org/10.2151/jmsj.84.277>.
- Nakamura, Y., and Y. N. Takayabu, 2022: Convective couplings with equatorial Rossby waves and equatorial Kelvin waves. Part I: Coupled wave structures. *J. Atmos. Sci.*, **79**, 247–262, <https://doi.org/10.1175/JAS-D-21-0080.1>.
- Nitta, T., 1972: Energy budget of wave disturbances over the Marshall Islands during the years of 1956 and 1958. *J. Meteor. Soc. Japan*, **50**, 71–84, https://doi.org/10.2151/jmsj1965.50.2_71.
- Raymond, D. J., and Ž. Fuchs, 2007: Convectively coupled gravity and moisture modes in a simple atmospheric model. *Tellus*, **59A**, 627–640, <https://doi.org/10.1111/j.1600-0870.2007.00268.x>.
- Rayner, N. A., D. E. Parker, E. B. Horton, C. K. Folland, L. V. Alexander, D. P. Rowell, E. C. Kent, and A. Kaplan, 2003: Global analyses of sea surface temperature, sea ice, and night marine air temperature since the late nineteenth century. *J. Geophys. Res.*, **108**, 4407, <https://doi.org/10.1029/2002JD002670>.
- Reichle, R. H., Q. Liu, R. D. Koster, C. S. Draper, S. P. Mahanama, and G. S. Partyka, 2017: Land surface precipitation in MERRA-2. *J. Climate*, **30**, 1643–1664, <https://doi.org/10.1175/JCLI-D-16-0570.1>.
- Ren, P., D. Kim, M. S. Ahn, D. Kang, and H. L. Ren, 2021: Intercomparison of MJO column moist static energy and water vapor budget among six modern reanalysis products. *J. Climate*, **34**, 2977–3001, <https://doi.org/10.1175/JCLI-D-20-0653.1>.
- Roundy, P. E., 2008: Analysis of convectively coupled Kelvin waves in the Indian Ocean MJO. *J. Atmos. Sci.*, **65**, 1342–1359, <https://doi.org/10.1175/2007JAS2345.1>.
- , and W. M. Frank, 2004: A climatology of waves in the equatorial region. *J. Atmos. Sci.*, **61**, 2105–2132, [https://doi.org/10.1175/1520-0469\(2004\)061<2105:ACOWIT>2.0.CO;2](https://doi.org/10.1175/1520-0469(2004)061<2105:ACOWIT>2.0.CO;2).
- Saha, S., and Coauthors, 2010: The NCEP Climate Forecast System Reanalysis. *Bull. Amer. Meteor. Soc.*, **91**, 1015–1058, <https://doi.org/10.1175/2010BAMS3001.1>.
- , and Coauthors, 2014: The NCEP Climate Forecast System version 2. *J. Climate*, **27**, 2185–2208, <https://doi.org/10.1175/JCLI-D-12-00823.1>.
- Sinclare, Z., A. Lenouo, C. Tchawoua, and S. Janicot, 2015: Synoptic Kelvin type perturbation waves over Congo basin over the period 1979–2010. *J. Atmos. Sol.-Terr. Phys.*, **130–131**, 43–56, <https://doi.org/10.1016/j.jastp.2015.04.015>.
- Straub, K. H., and G. N. Kiladis, 2002: Observations of a convectively coupled Kelvin wave in the eastern Pacific ITCZ. *J. Atmos. Sci.*, **59**, 30–53, [https://doi.org/10.1175/1520-0469\(2002\)059<0030:OOACCK>2.0.CO;2](https://doi.org/10.1175/1520-0469(2002)059<0030:OOACCK>2.0.CO;2).
- , and —, 2003a: Extratropical forcing of convectively coupled Kelvin waves during austral winter. *J. Atmos. Sci.*, **60**, 526–543, [https://doi.org/10.1175/1520-0469\(2003\)060<0526:EFOCCK>2.0.CO;2](https://doi.org/10.1175/1520-0469(2003)060<0526:EFOCCK>2.0.CO;2).
- , and —, 2003b: The observed structure of convectively coupled Kelvin waves: Comparison with simple models of coupled wave instability. *J. Atmos. Sci.*, **60**, 1655–1668, [https://doi.org/10.1175/1520-0469\(2003\)060<1655:TOSOCC>2.0.CO;2](https://doi.org/10.1175/1520-0469(2003)060<1655:TOSOCC>2.0.CO;2).
- , —, and P. E. Ciesielski, 2006: The role of equatorial waves in the onset of the South China Sea summer monsoon and the demise of El Niño during 1998. *Dyn. Atmos. Oceans*, **42**, 216–238, <https://doi.org/10.1016/j.dynatmoce.2006.02.005>.
- , P. T. Haertel, and G. N. Kiladis, 2010: An analysis of convectively coupled Kelvin waves in 20 WCRP CMIP3 global coupled climate models. *J. Climate*, **23**, 3031–3056, <https://doi.org/10.1175/2009JCLI3422.1>.
- Tulich, S. N., and G. N. Kiladis, 2021: On the regionality of moist Kelvin waves and the MJO: The critical role of the background zonal flow. *J. Adv. Model. Earth Syst.*, **13**, e2021MS002528, <https://doi.org/10.1029/2021MS002528>.
- Wang, H., and R. Fu, 2007: The influence of Amazon rainfall on the Atlantic ITCZ through convectively coupled Kelvin waves. *J. Climate*, **20**, 1188–1201, <https://doi.org/10.1175/JCLI4061.1>.
- Wang, L., and L. Chen, 2016: Interannual variation of convectively coupled equatorial waves and their association with environmental factors. *Dyn. Atmos. Oceans*, **76**, 116–126, <https://doi.org/10.1016/j.dynatmoce.2016.10.004>.
- Wheeler, M., and G. N. Kiladis, 1999: Convectively coupled equatorial waves: Analysis of clouds and temperature in the wavenumber-frequency domain. *J. Atmos. Sci.*, **56**, 374–399, [https://doi.org/10.1175/1520-0469\(1999\)056<0374:CCEWAO>2.0.CO;2](https://doi.org/10.1175/1520-0469(1999)056<0374:CCEWAO>2.0.CO;2).
- Yanai, M., S. Esbensen, and J.-H. Chu, 1973: Determination of bulk properties of tropical cloud clusters from large-scale heat and moisture budgets. *J. Atmos. Sci.*, **30**, 611–627, [https://doi.org/10.1175/1520-0469\(1973\)030<0611:DOBPO>2.0.CO;2](https://doi.org/10.1175/1520-0469(1973)030<0611:DOBPO>2.0.CO;2).
- Yang, G.-Y., B. Hoskins, and J. Slingo, 2007: Convectively coupled equatorial waves. Part I: Horizontal and vertical structures. *J. Atmos. Sci.*, **64**, 3406–3423, <https://doi.org/10.1175/JAS4017.1>.
- Yasunaga, K., 2011: Seasonality and regionality of the Madden-Julian oscillation and convectively coupled equatorial waves. *SOLA*, **7**, 153–156, <https://doi.org/10.2151/sola.2011-039>.
- , and B. Mapes, 2012: Differences between more divergent and more rotational types of convectively coupled equatorial waves. Part I: Space-time spectral analyses. *J. Atmos. Sci.*, **69**, 3–16, <https://doi.org/10.1175/JAS-D-11-033.1>.